Global Sensitivity Analysis to Optimize Basin-Scale Conductive Model Calibration – Insights on the Upper Rhine Graben

Denise Degen[a,b,*], Karen Veroy[a,c,d], Jessica Freymark[e,f], Magdalena Scheck-Wenderoth[e,f], Florian Wellmann[b]

[a]*Aachen Institute for Advanced Study in Computational Engineering Science (AICES), RWTH Aachen University, Schinkelstraße 2, 52062 Aachen, Germany*
[b]*Computational Geoscience and Reservoir Engineering (CGRE), RWTH Aachen University, Wüllnerstraße 2, 52072 Aachen, Germany*
[c]*Faculty of Civil Engineering, RWTH Aachen University, Aachen, Germany*
[d]*Centre for Analysis, Scientific Computing, and Applications W&I, TU Eindhoven, PO Box 513, 5600 MB Eindhoven, Netherlands*
[e]*Faculty of Georesources and Materials Engineering, RWTH Aachen University, Aachen, Germany*
[f]*GFZ German Research Centre for Geosciences, Telegrafenberg, 14473 Potsdam, Germany*

Abstract

Geothermal simulations are widely used in both scientific and applied industrial contexts. Typically, the temperature state is evaluated on the basis of the heat equation, with suitable parameterizations of the model domain and defined boundary conditions, which are calibrated to obtain a minimal misfit between measured and simulated temperature values. We demonstrate the essential need for global sensitivity studies for robust geothermal model calibrations since local studies overestimate the influence of the parameters. We ensure the feasibility of the study by using a physics-based machine learning approach, that reduces the computation time by several orders of magnitude.

Keywords: global sensitivity analysis, sensitivity-driven model calibration, Upper Rhine Graben, reduced basis method

---

*Corresponding author

1. Introduction

Physical process simulations are used in a wide range of geothermal studies - from the investigation of global and regional temperature fields, to local reservoir studies (Cacace et al., 2013; Kolditz & Clauser, 1998; Konrad et al., 2019; Randolph & Saar, 2011). As in many geoscientific applications, these simulations are based on models with associated uncertainties in the selection of the physical model (conductive, hydrothermal, mechanical, etc.) and of the relevant parameters (hydraulic and thermal conductivities, radiogenic heat production, etc.). To compensate for these model errors, arising from, for instance, measurement errors, generalizations, and geometrical uncertainties (Houghton et al., 2001; Murphy et al., 2004; Refsgaard et al., 2007; Wellmann & Caumon, 2018), we need model calibrations to obtain reliable and robust models. Here, we investigate the requirement and potential of sensitivity analyses and automated model calibrations for regional conductive heat flow models on the basin scale, with an application to the Upper Rhine Graben in Central Europe.

Reliable and robust model calibrations are a challenge for deep geothermal systems because most temperature measurements are at a shallow depth. Typically, only a limited number of deeper measurements is available for the model validation. This imbalance has an important influence on the ability to identify uncertain model parameters: if a model parameter only has a very limited influence on the output value at the position of the available data points, then, similarly, it will not be possible to estimate this parameter from the available data. The analysis of parameters that can be identified and calibrated is the main goal of the field of sensitivity analysis (Saltelli et al., 2004).

Sensitivity analyses (SA) can be categorized into local and global analyses (Saltelli et al., 2004; Wainwright et al., 2014). In the work presented here, we investigate both local and global approaches and evaluate specifically the requirement and added value of global SA for regional geothermal simulation studies on the scale of an entire basin.

This investigation is important since local SA have known deficiencies as

they are only locally investigating the first-order parameter influence around a given parameter set. In geothermal applications, the parameters sets (e.g., thermal conductivities, and radiogenic heat productions) are usually associated with high uncertainties (Freymark et al., 2017; Lehmann et al., 1998; Vogt et al., 2010; Wagner & Clauser, 2005). These high uncertainties quickly lead to wrong initial guesses of the various parameters bearing the high risk of exploring the wrong part of the parameter space with a local sensitivity analysis. Based on this realization, global SA have been developed (see Saltelli et al., 2004, for an overview), but these typically require many thousand forward simulations and are therefore often infeasible for more complex or larger simulations, where a single simulation run can require tens of minutes or even hours of simulation time.

To overcome the problem of the long simulation time, and to make global SA possible for geothermal conductive heat flow models, we apply here the reduced basis (RB) method to obtain a highly efficient surrogate model for the entire forward simulation. The RB method is essentially a physics-based machine learning approach (Hesthaven et al., 2016; Prud'homme et al., 2002). This method has been adapted successfully for geophysical simulations (Degen et al., 2020) and showed promising results with a reduction of simulation time by several orders of magnitude, after model training, while still providing highly accurate estimates of state variables at measurement locations. We will apply this method here to make a global SA feasible and to efficiently test several model scenarios.

Global sensitivity analyses in geosciences have been performed for hydrological studies (van Griensven et al., 2006; Tang et al., 2007; Cloke et al., 2008; Zhan et al., 2013; Baroni & Tarantola, 2014; Song et al., 2015), for volcanic source modeling (Cannavó, 2012), and for geothermal heat exchangers (Fernández et al., 2017). Furthermore, a comparison of local and global sensitivity analysis has been performed for a hydrological model in Wainwright et al. (2014). However, there is no comparison of local and global sensitivity analyses for basin-scale geothermal heat flow models available yet, as presented here,

with a focus also on the uneven distribution of measurement points.

We apply the approach here to a case study of the Upper Rhine Graben and its surrounding region, Central Europe. This region has gained significant interest for deep geothermal exploration due to its increased geothermal gradient, for example around Soultz-sous-Forêts, Landau, and Bruchsal (Agemar et al., 2013, 2014; Illies, 1972; Pauwels et al., 1993; Geothermie, 2007; Vidal et al., 2015). However, obtaining reliable spatial temperature distributions is a major challenge as seen in the ongoing discussion in literature (Agemar et al., 2013, 2014; Freymark et al., 2017, 2019; GeORG-Projektteam, 2013; Stober & Bucher, 2015), also because of the unclear influence of advection on the temperature distribution within the Upper Rhine Graben. So far, only "trial-and-error" model calibrations have been performed in basin-scale models of this region (Freymark et al., 2017). With this work, we aim to contribute with a detailed global SA, followed by a full calibration of a conductive geothermal model, and identify the suitability of such a model in different regions of the basin.

The paper is structured as follows: We provide an overview of the numerical methods, including sensitivity analyses, model calibrations, and the reduced basis method in Section 2. This is followed by a comparison of various model calibrations, considering different sensitivity analysis techniques and different data weighting schemes for the Upper Rhine Graben in Section 3. We discuss the results in Section 4 and present concluding remarks in Section 5.

2. Materials and Methods

In the following, we briefly demonstrate the concepts of both local and global sensitivity analysis through a simplified geological basin-scale model. The presentations of the physical model, the RB method, and the concepts of model calibration follow.

2.1. Sensitivity Analysis

Consider a function $u = f(x)$, where $x = (x_1, ..., x_N)$ are the model parameters and let $u^* = f(x^*)$ be the desired solution, then the sensitivity analysis aims

to determine the influence of the model parameters x on the model $f(x)$ (Sobol, 2001; Wainwright et al., 2014). The evaluation of these sensitivities differs for the local and global sensitivity analysis, as discussed in the next sections. The sensitivity analysis is a natural preparation step for a model calibration (Ray et al., 2015). As we demonstrate in this paper, the efficient reduction of the parameter state leads to more robust model calibration results.

As described in the introduction, the sensitivity analysis can be subdivided into a local and global study (Sobol, 2001). In the following, we will briefly describe the main difference between both analyses. We illustrate the concepts by using a simplified geological basin-scale model (Fig. 2.1). We use the same governing equations subsequently for the case study. The top boundary condition is set to 10 °C, which corresponds to the annual average surface temperature in Germany (Deutscher Wetterdienst, 2020). The bottom boundary condition is set to the 1300 °C isotherm since the lower model boundary is assumed to correspond to the thermal lithosphere-asthenosphere boundary (LAB) (Turcotte & Schubert, 2002). The model extends 292 km in the x-direction, 525 km in the y-direction and -80 km in the z-direction, in agreement with the dimensions of the Upper Rhine Graben model (Freymark et al., 2017). The parameter values are taken from Freymark et al. (2017), and the top layer corresponds to the Cenozoic Volcanics, the middle layer to the Saxothuringian, and the bottom layer to the Lithospheric Mantle. We investigate the sensitivities of all thermal conductivities and the radiogenic heat production of the Saxothuringian. Note that we perform the simulation with the nondimensional equation for investigating the relative importance of the model parameters and for efficiency reasons. For details regarding the nondimensional model refer to Section 2.2. Hence, we have nondimensional temperatures between -1 and 0.Additionally, we apply, for efficiency reasons, a lifting function removing the static effects of the lower boundary condition.
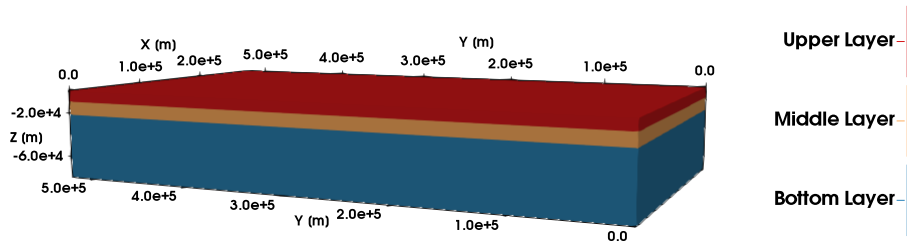
Figure 2.1: Simplified basin-scale model for illustrating the concepts of the methods presented in this chapter.

2.1.1. Local Sensitivity Analysis

If we consider again the function $u = f(x)$, with $x = (x_1, ..., x_N)$ being the model parameters, and the desired solution $u^* = f(x^*)$, then for the local sensitivity analysis, we evaluate the sensitivity by taking $\left(\frac{\partial u}{\partial x_k}\right)_{x=x^*}$. Hence, the local SA investigates the influence of the various model parameters with respect to a pre-defined reference parameter set. For this reason, they focus on the sensitivity in the vicinity of the input parameters (Sobol, 2001; Wainwright et al., 2014). Hence, in case of the local sensitivity analysis, we allow a defined variation of, e.g., 1 %. The local sensitivity analysis does not consider parameter correlations. It assumes that the influence observed for each realization is solely arising from the single changed model parameter.

In case of a geothermal application, we would, for instance, determine the influence of the different thermal conductivities with respect to a reference set, which would usually be our initial guess. That already shows the major issue with local sensitivity analyses: we have to define a reference. With this reference parameter set, we calculate the reference temperatures at our observation points, using our physical model. These reference temperatures are, however, not identical to our observed temperatures due to model and measurement errors. To conclude, we have to use our "best" knowledge as the reference. If we consider the uncertainties related to geothermal applications this "best" knowledge likely does not represent the "true" parameter values. Therefore, we introduce an error in the sensitivity analysis that can lead to wrong and possibly

misleading estimates of parameter sensitivities.

For our simple basin-scale model, we obtain the sensitivities presented in Fig. 2.2. As mentioned, we need to define a reference parameter set for the local sensitivity study. For this reference set, we take the calibrated values presented in Freymark et al. (2017). We investigate the influence of the model parameters on the absolute misfit between the simulated and the reference temperature data. Using the observed temperatures instead of the reference temperatures leads to equal sensitivities for all parameters because these temperatures lie outside the 1 % variation range. For the comparison with the reference temperatures, we observe that the model is sensitive to all investigated parameters assuming a threshold of 10^{-1}. For further analyses, this means that we would have to consider all model parameters.

2.1.2. Global Sensitivity Analysis

For the global analysis, we use the Sobol sensitivity analysis with the Saltelli sampler, which is a variance-based sensitivity analysis (Sobol, 2001; Saltelli, 2002; Saltelli et al., 2010; Wainwright et al., 2014). It does not set $x = x^*$, but evaluates instead the entire model $f(x)$. Assuming a square-integrable function, with orthogonal members, we can decompose it into the following form (Sobol, 2001):

$$\int f^2(x)\mathrm{d}x - f_0^2 = \sum_{s=1}^{n} \sum_{i_1 < \cdots < i_s}^{n} \int f_{i_1 \cdots i_s}^2 \mathrm{d}x_{i_1} \cdots \mathrm{d}x_{i_s}, \qquad (1)$$

where $1 \leq i_1 < \cdots < i_s \leq n$, f_0 is a constant, and f_i a function. Eq. 1 can be rewritten as:

$$\int f^2(x)\mathrm{d}x - f_0^2 = \sum_i \int f_i^2(x_i) + \sum_{i<j} \int f_{ij}^2(x_i, x_j) + \cdots + \int f_{12\cdots n}^2(x_1, x_2, \cdots, x_n). \qquad (2)$$

The variances D are then defined as (Sobol, 2001):

$$D = \int f^2 \mathrm{d}x - f_0^2, \qquad D_{i_1 \cdots i_s} = \int f_{i_1 \cdots i_s}^2 \mathrm{d}x_{i_1} \cdots \mathrm{d}x_{i_s}. \qquad (3)$$
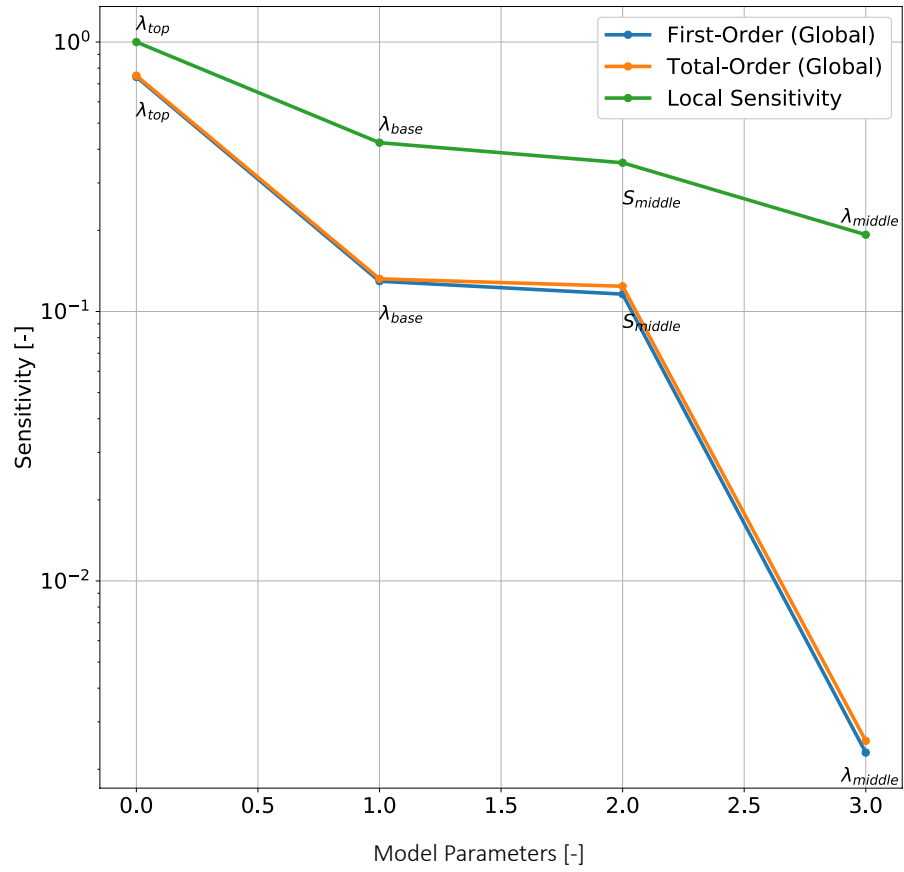
Figure 2.2: We present a comparison of the local and global sensitivity analysis for the benchmark problem. The local sensitivity indices are denoted in green, the first-order contributions (global sensitivity analysis) in blue, and the total-order contributions (global sensitivity analysis) in orange.

The global sensitivity indices S can be derived from the variances by taking the ratio (Sobol, 2001):

$$S_{i_1 \cdots i_s} = \frac{D_{i_1 \cdots i_s}}{D}. \qquad (4)$$

We use the global sensitivity analyses to investigate the influence of the model parameters on the total absolute misfit between the simulated and the observed temperature data. In contrast to the local SA, the global SA does not require a reference and investigates the influences of all parameters within the pre-defined parameter ranges (Sobol, 2001). Hence, we are no longer restricted to small parameter variations. Furthermore, we no longer need to know the parameter distribution in advance and only specify an allowable physical range.

The first-order index represents the influence on the model of the model parameter itself. The second-order index describes the influence of the correlation between two parameters. Further, higher-order indices are available to investigate the influence of the correlation between more than two parameters (Sobol, 2001). For further details regarding the definition of the sensitivity indices, we refer to Sobol (2001), and for further information regarding the sampling procedure, we refer to Saltelli (2002), and Saltelli et al. (2010).

In the practical example of the geothermal simulation considered here, this means that we no longer need to specify our possibly wrong "best" knowledge of the thermal properties. We performed the global sensitivity analysis for the simple basin-scale model (Fig. 2.2), where we use 10,000 realizations per parameter to reduce the statistical error to eliminate negative sensitivities yielding a computationally extremely demanding analysis. To compensate for this high computational costs, we employ the reduced basis method to construct a fast, physics-preserving and highly accurate surrogate model. The sensitivity analysis is executed using the Python library SALib (Herman & Usher, 2017). The results significantly differ from the ones of the local sensitivity analysis: we still observe the dominant influence from the thermal conductivity of the top layer. However, we see that the model is insensitive to the thermal conductivity of the middle layer. So, the local sensitivity analysis overestimates the influence of this

model parameter. Furthermore, the local analysis overestimates the influence of both the thermal conductivity of the bottom layer and the radiogenic heat production of the middle layer. So, in contrast to the local sensitivity analysis, we can reduce the dimension of the parameter space from four to three.

In addition to the total sensitivities, we obtain the information about the parameter correlations. For the presented model, we observe nearly exclusive first-order contributions. Hence, the parameter correlations in the presented model are small. The local sensitivity analysis already fails for this model, even it is ideally suited for it since it has negligible parameter correlations. However, the global sensitivity analysis has the issue that it requires many forward simulations. In Section 3, we describe how we overcome this disadvantage.

2.2. Forward Simulation

For the forward simulations of the temperatures, we consider a steady-state geothermal heat conduction problem with a radiogenic heat production after Bayer et al. (1997).

$$-\lambda \nabla^2 T + S = 0, \tag{5}$$

where λ is the thermal conductivity, T the temperature and S the radiogenic heat production. We are taking only nondimensional parameters and variables into account, which leads to Eq. 6:

$$-\frac{\lambda}{\lambda_{\mathrm{ref}}\ S_{\mathrm{ref}}}\ \frac{\nabla^2}{l_{\mathrm{ref}}^2}\ (\frac{T - T_{\mathrm{ref}}}{T_{\mathrm{ref}}})\ +\ \frac{S\ l_{\mathrm{ref}}^2}{S_{\mathrm{ref}}\ T_{\mathrm{ref}}\ \lambda_{\mathrm{ref}}}\ =\ 0 \tag{6}$$

Here, λ_{ref} is the reference thermal conductivity, T_{ref} the reference temperature, S_{ref} the reference radiogenic heat production, and l_{ref} the reference length.

2.3. Model Calibration

Based on the results of the sensitivity study, we perform model calibrations on the most sensitive parameters only. The threshold is defined as 10^{-1} analog to the case study of the Upper Rhine Graben (Section 3).

We consider the trust region reflective (TRF) method from SciPy (Branch et al., 1999; Jones et al., 2014) as our calibration method since it is robust

and considers bounds for the model parameters (Jones et al., 2014). Especially the latter aspect is of utmost importance since our surrogate models are only valid if we remain within the pre-defined training ranges. This is the reason why we cannot use the conjugate gradient method provided by SciPy. The implementation of SciPy does not allow the consideration of bounds for the model parameters.

Take the following problem into account: $\min_{x \in \mathbb{R}^n} \{f(x) : \quad l \leq x \leq u\}$, where we want to minimize the function $f(x)$ with x being our model parameter. Furthermore, the model parameters are bounded below by the lower bound l, and above by the upper bound u. The method defines a trust region N around the current "best" solution to improve the convergence rate. In standard trust region methods, the quadratic model $q(s)$ is assumed to approximate the original objective function inside the trust region. We derive the quadratic model by taking the first two steps of the Taylor expansion of f at x. The trial step s is computed by minimizing over the trust region: $\min_{s}\{q(s), s \in N\}$. The current point is updated to $x + s$ if $f(x + s) < f(x)$ and the trust region is updated. If we do not fulfill this condition, the current point stays the same. Then, we decrease the trust region and repeat the computation of the trial step. The trust region optimization problem is then expressed as: $\min \left\{ \frac{1}{2} s^T H s + s^T g \text{ such that } \|Ds\| \leq \Delta \right\}$. Here, g is the gradient, H the Hessian matrix, D a diagonal scaling matrix, and Δ a positive scalar. We repeat these steps until we reach convergence. Minimizing a quadratic function – instead of the original, possibly non-linear, objective function – results in a reduction in compute time. More details about the method can be found in Branch et al. (1999).

3. Case Study of the Upper Rhine Graben

In the next section, we use the Upper Rhine Graben, presented in Freymark et al. (2017), as a case study to illustrate the benefits of a combined global sensitivity study and a model calibration. This is used to optimize the temperature

predictions of real-case basin-scale conductive heat flow models.

3.1. Upper Rhine Graben – High Fidelity Model

This paper uses the model of the Upper Rhine Graben presented in Freymark et al. (2017), and in this section, we give an introduction into its numerical aspects.
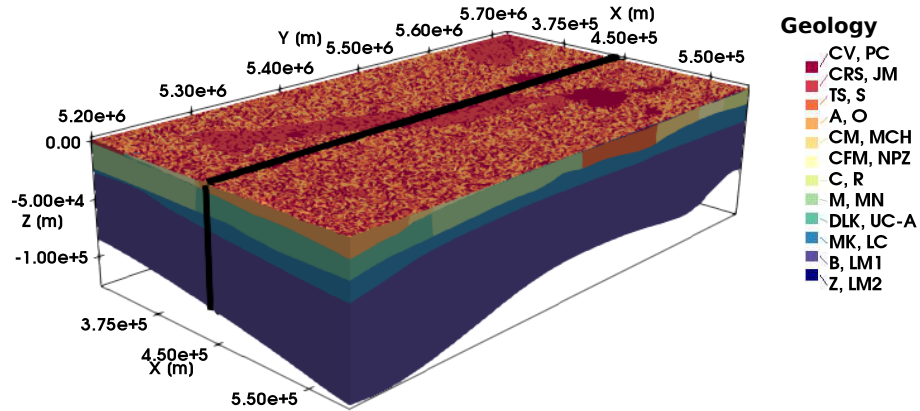

Figure 3.1: Image of the geology of the Upper Rhine Graben. The cross-section that is later on used for visualizing the sensitivities is indicated by a black line. The acronyms for the respective geological layers are defined in Tab. 1.

The model (Fig. 3.1) extends 292 km in the x-direction, 525 km in the y-direction, and in the vertical direction down to the lithosphere-asthenosphere boundary. It consists of 24 geological layers and is discretized using deformed eight-noded prisms. The horizontal resolution is one km, and the vertical resolution corresponds to the layer thickness yielding 3,852,950 degrees of freedom. At the top and the bottom of the model, we apply Dirichlet boundary conditions, and we set all lateral boundaries to no-flow boundaries. For the upper boundary condition, we use the annual average surface temperatures, as presented in Freymark et al. (2017). In contrast, the lower boundary condition is set to 1300 °C isotherm at the LAB (Turcotte & Schubert, 2002).

12

3.2. Data and Weighting

Data are very unequally distributed throughout the spatial domain. In order to compensate for this inequality, we introduce weights. For the calculation of the weights, we consider two ways: First, we calculate them automatically via a distance matrix provided by SciPy, and second we specify them via user-input. The user-defined weighting is obtained by splitting the data into three regions (Fig. 3.2). We see that in region 3, corresponding to the northern part of the Upper Rhine Graben, we have only very few data points. To compensate for the data sparsity in this region, we apply a weight of 10 to the misfit. Many observation data are available in the Hesse area, while significantly fewer data are available for the Upper Rhine Graben. In order to compensate for this unequal data distribution, we apply a weight of 0.1 to region 1 and of 1.0 to region 2.
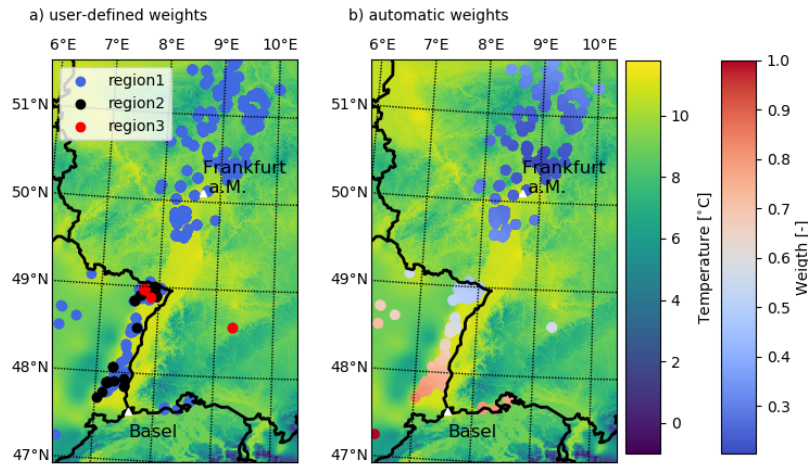

Figure 3.2: Comparison of the distribution of the weights for the automated model calibration. On the left side is the distribution derived from expert knowledge, and on the right side the weighting scheme using the distance matrix.

3.3. Upper Rhine Graben – Low Fidelity Model

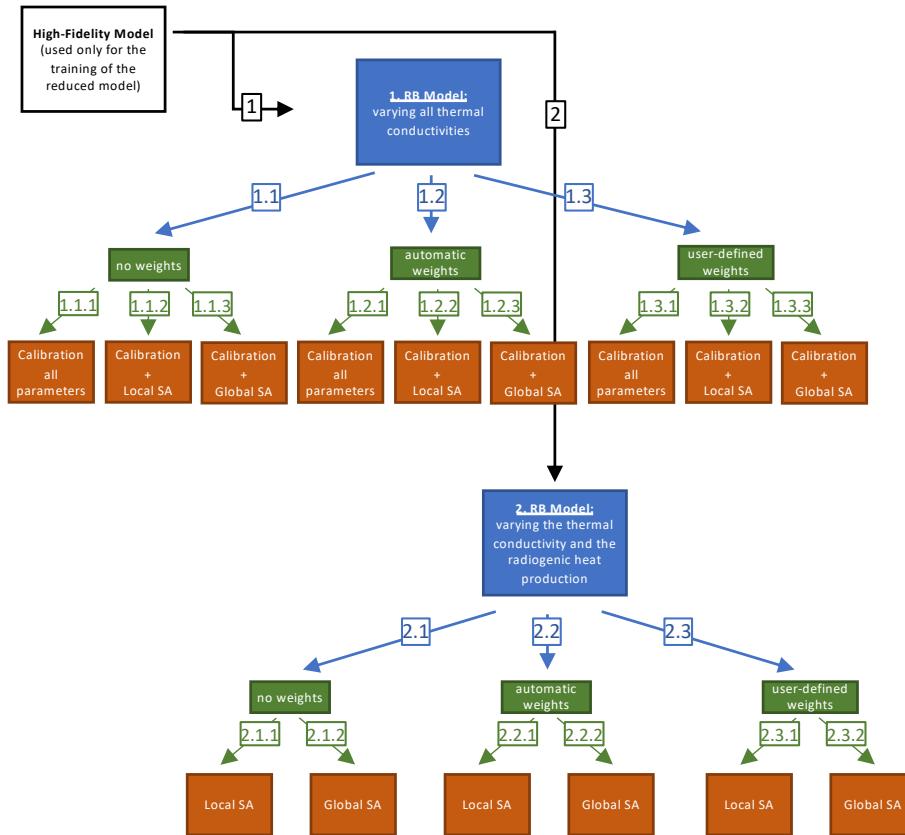Based on the full FE model, we constructed two reduced models:

Figure 3.3: Overview of the various model scenarios used for the model calibrations and sensitivity analyses of the Upper Rhine Graben.

- The first one (branch 1 of Fig. 3.3) considers only thermal conductivities as model parameters. It consists of 12 different parameters since we combined the layers with equal thermal conductivities into one.

- The second one (branch 2 of Fig. 3.3) contains the thermal conductivity of the Cenozoic Rift Sediments and the radiogenic heat productions from the Upper Crust, resulting in eight parameters.

In both models, we define the allowed variations of the parameters in accordance with the ranges given in Freymark et al. (2017). If no range is defined in Freymark et al. (2017), we allow a variation of $\pm$ 50 % from the initial value.

For the nondimensional representation of the Upper Rhine Graben model, we set the reference thermal conductivity λ_{ref} to the maximum thermal conductivity of 6.0 W m^{-1} K^{-1}. Analog, we choose the maximum temperature of 1300 °C as the reference temperature T_{ref} and the maximum radiogenic heat production of 3.0 μW m^3 as the reference radiogenic heat production S_{ref}. The reference length l_{ref} corresponds to the maximum y-extent of the mesh (525,000 m).

We are using the RB solution as a surrogate model for the FE method. In order to apply the method, we need to decompose the PDE into its parameter-dependent and -independent part. This leads to the following decomposition of the bilinear form a for both reduced models:

$$a(w, v; \lambda) = -\sum_{q=0}^{n} \lambda_q \int_{\Omega} \nabla w \ \nabla v \ d\Omega, \qquad \forall v, w \in X, \ \forall \lambda \in \mathcal{D}. \qquad (7)$$

Here, w is the trial function, v the test function, the index "q" denotes the number of the training parameters (see also Tab. 1 – 3), X the function space ($H_0^1(\Omega) \subset X \subset H_1(\Omega)$), Ω the spatial domain in $\mathbb{R}^3$, and $\mathcal{D}$ the parameter domain in $\mathbb{R}^{12}$. For the reduced model with varying thermal conductivities (branch 1 of Fig. 3.3) n is equal to 11 and for the one with varying thermal conductivities and radiogenic heat production (branch 2 of Fig. 3.3) n is equal to one.

The decomposed linear form f has the following form for the first reduced model (branch 1 of Fig. 3.3):

$$f(v; \lambda) = -\sum_{q=0}^{11} \lambda_q \int_{\Gamma} \nabla v \ g(x, y, z) \ d\Gamma +$$

$$\int_{\Gamma} \nabla v \ S \ d\Gamma, \qquad \forall v \in X, \ \forall \lambda \in \mathcal{D}, \qquad (8)$$

$$\text{with g(x, y, z)} = T_{top} \frac{h(x, y, z) - z_{bottom}(x, y)}{d(x, y)},$$

where Γ is the boundary in $\mathbb{R}^3$, $g(x, y, z)$ the lifting function, T_{top} the temperature at the top of the model, $h(x, y, z)$ the location in the model, $z_{bottom}(x, y)$ the depth of the bottom surface, and $d(x, y)$ the distance between the bottom and top surface.

The decomposition of the linear form of the second reduced model (branch 2 of Fig. 3.3) is similar:

$$f(v; \lambda) = - \int_{\Gamma} \lambda_{(1)} \nabla v \ g(x,y,z) \ d\Gamma - \lambda_1 \int_{\Gamma} \nabla v \ g(x,y,z) +$$
$$d\Gamma \int_{\Gamma} \nabla v \ S_{(14-20)} \ d\Gamma + \sum_{q=14}^{20} S_q \int_{\Gamma} \nabla v \ d\Gamma, \quad \forall v \in X, \ \forall \lambda \in \mathcal{D},$$

with $g(x, y, z) = T_{top} \dfrac{h(x,y,z) - z_{bottom}(x,y)}{d(x,y)}.$

$$(9)$$

Here, $\lambda_{(1)}$ are all thermal conductivities except the thermal conductivity of the Cenozoic Rift Sediment, λ_1 the thermal conductivity of the Cenozoic Rift Sediments, S_{14-20} the radiogenic heat productions of the upper crust layers, and $S_{(14-20)}$ all remaining radiogenic heat productions.

3.4. Model Calibration without Sensitivity Analysis

For all calibrations (branches 1.1.1 to 1.3.3 of Fig. 3.3), we only vary the thermal conductivities since the influence of the radiogenic heat production is negligible in comparison to the thermal conductivity. We demonstrate this in the following sections. As the loss function, we use the smooth approximation of the L1 absolute value loss with a value of 0.1 for the soft margin between inlier and outlier residuals. We set the tolerances for the termination to 10^{-5} for changes of the cost function, 10^{-8} for the norm of the gradient, and 10^{-5} for changes of the independent parameters. We perform the calibration three times, once without weighing the misfit of observed and simulated data and once with applying the different weighting methods to the misfit (branches 1.1 to 1.3 of Fig. 3.3).

Furthermore, note that all forward simulations throughout all model calibrations and sensitivity analyses are performed with the reduced model to speed-up the analysis time and to make the global sensitivity study feasible.

If we do not incorporate any sensitivity result into the model calibration, we have to calibrate our model with all thermal conductivities consequently (branches 1.1.1, 1.2.1, and 1.3.1 of Fig. 3.3). Tab. 1 summarizes the parameter

values for all considered scenarios. The result from the model calibration without weights (branch 1.1.1 of Fig. 3.3) and the model calibration with automatic weights (branch 1.2.1 of Fig. 3.3) are very similar.

Significant differences are observed for the model calibration with user-defined weights (branch 1.3.1 of Fig. 3.3). The major differences occur for the Cenozoic Volcanics and Rift Sediments and the Lithospheric Mantle. The Cenozoic Volcanics and Rift Sediments show a decrease in thermal conductivity to the initial values for the model calibration with user-defined weights, and the other two show an increase. The decrease for the Cenozoic Rift Sediments in case of the model calibration with user-defined weights is with 0.4 W m^{-1} K^{-1} enormous, and also the increase in thermal conductivity of 0.9 W m^{-1} K^{-1} for the Cenozoic Volcanics for the model calibration without and with automatic weights.

Also, for the Cenozoic Folded Molasse/Cenozoic Foreland Molasse/Buntsandstein/Jura Mountains/Odenwald, the Dogger/Lias/Keuper/Saxothuringian /Moldanubian, the Muschelkalk, the Zechstein/Upper Crust - Alps, and the Mid-German Crystalline High, significant differences in the calibrated thermal conductivities are observed. The model calibrations without weights and with automatic weights follow the same trend, whereas the model calibration with user-defined weights mostly follows the reversed trend. The other layers show similar calibrated model parameters for all model calibration versions.

Furthermore, for all three versions of the model calibration (branches 1.1.1, 1.2.1, and 1.3.1 of Fig. 3.3), many of the calibrated model parameters reach the upper or lower bound of their pre-defined variation range, as indicated in Tab. 1.

Table 1: The thermal properties before and after the calibration for the Upper Rhine Graben without considering the results of a sensitivity study. The initial thermal properties are taken from Freymark et al. (2017). Note that UC stands for Upper Crust, ub for upper bound, and lb for lower bound.

ID	Layer	Training Parameter	Initial Bulk Thermal Conductivity [W m⁻¹ K⁻¹]	Calibrated Thermal Conductivity [W m⁻¹ K⁻¹]			Radiogenic Heat Production [$\mu W m^{-3}$]
				user-defined weights	automatic weights	no weights	
CV	Cenozoic Volcanics	0	1.8	1.6	2.7 (ub)	2.7 (ub)	0.2
CRS	Cenozoic Rift Sediments	1	1.2	0.8	1.4	1.4	1.0
TS	Tertiary salt	2	6.0	5.5 (lb)	5.5 (lb)	5.5 (lb)	0.0
A	Alps	3	2.2	1.3	1.4	1.5	0.3
CM	Cenozoic Folded Molasse	4	3.0	4.5 (ub)	3.4	3.5	1.0
CFM	Cenozoic Foreland Molasse	4	3.0	4.5 (ub)	3.4	3.5	1.0

18

C	Cretaceous	3	2.2	1.3	1.4	1.5	0.5
M	Malm	5	2.7	2.8 (ub)	2.8 (ub)	2.8 (ub)	1.4
DLK	Dogger/Lias/Keuper	6	2.5	2.4 (lb)	3.2	3.5 (ub)	1.6
MK	Muschelkalk	7	2.0	3.0 (ub)	2.1	1.5	1.2
B	Buntsandstein	4	3.0	4.5 (ub)	3.4	3.5	1.0
Z	Zechstein	8	2.3	2.5	3.4 (ub)	3.4 (ub)	0.8
PC	Permo-Carboniferous	3	2.2	1.3	1.4	1.5	1.0
JM	Jura Mountains	4	3.0	4.5 (ub)	3.4	3.5	0.5
S	UC: Saxothuringian	6	2.5	2.4 (lb)	3.2	3.5 (ub)	2.5
O	UC: Odenwald	4	3.0	4.5 (ub)	3.4	3.5	1.8
MCH	UC: Mid-German Crystalline High	9	2.4	2.7 (ub)	2.3 (lb)	2.3 (lb)	1.8
NPZ	UC: Nothern Phyllite Zone	5	2.7	2.8 (ub)	2.8 (ub)	2.8 (ub)	3.0

R	UC: Rheno-hercynian	5	2.7	2.8 (ub)	2.8 (ub)	2.8 (ub)	1.0
MN	UC: Moldanu-bian	6	2.5	2.4 (lb)	3.2	3.5 (ub)	2.6
UC-A	UC: Alps	8	2.3	2.5	3.4 (ub)	3.4 (ub)	2.4
LC	Lower Crust	10	2.1	2.1 (lb)	2.3	2.1 (lb)	0.5
LM1	Lithospheric Mantle 1	11	3.95	4.1	5.9 (ub)	5.9 (ub)	0.03
LM2	Lithospheric Mantle 2	11	3.95	4.1	5.9 (ub)	5.9 (ub)	0.03

3.5. Model Calibration with Local Sensitivity Analysis

In this section, we investigate the model calibration of the Upper Rhine Graben under consideration of a local sensitivity analysis again with all three model weighting versions (branches 1.1.2, 1.2.2, and 1.3.2 of Fig. 3.3). First, we present the sensitivity results, and then we show how to incorporate these results into the model calibration procedure.

3.5.1. Sensitivity Analysis

The results of the local sensitivity analyses are shown in Fig. 3.4 for all parameters sorted by decreasing influence and in Fig. 3.5 in a cross-sectional view.

The local sensitivity analysis without weights (for the reduced model with varying thermal conductivities – branch 1.1.2 of Fig. 3.3) has high sensitivities for the thermal conductivities of the Cenozoic Rift Sediments and the Lithospheric Mantle. Also, the Cenozoic Folded Molasse/Cenozoic Foreland

Molasse/Buntsandstein/Jura Mountains/Odenwald layers have a significant influence on the model response. The influences of the Malm/Northern Phyllite Zone/Rhenohercynian, the Mid-German Crystalline High, and the Lower Crust have a comparable influence on the model response. This influence is the third highest from all model parameters. The last parameter that influences the model is the thermal conductivity of the Cenozoic Volcanics. The remaining layers have a sensitivity below 0.1 and are for the further analyses not considered.

The sensitivities for the case with automatic weights (branch 1.2.2 of Fig. 3.3) are similar except that now also the Cenozoic Volcanics are insensitive to the temperature distribution. For the analyses with user-defined weights (branch 1.3.2 of Fig. 3.3), we observe slightly smaller sensitivities for all parameters except the sensitivity of the thermal conductivity of the Cenozoic Rift Sediments. Now also the Malm/Northern Phyllite Zone/Rhenohercynian layers do not influence the temperature distribution.

For the local sensitivity analysis, using the reduced model with varying thermal conductivity and radiogenic heat production rates (branches 2.1.1, 2.2.1, and 2.3.1 of Fig. 3.3, and Fig. 3.6), we see again that the highest sensitivity is arising from the thermal conductivity of the Cenozoic Rift Sediments. The sensitivities form the radiogenic heat productions of the Upper Crust are significantly lower. These results are independent of the weighting scheme.

For the analysis without weights (branch 2.1.1 of Fig. 3.3), we obtain similar sensitivities for the radiogenic heat productions of the Saxothuringian, the Mid-German Crystalline High, the Northern Phyllite Zone, and the Moldanubian. The one of the Rhenohercynian is significantly lower, and the those of the Odenwald and Alps are negligible.

In case of the local sensitivity analysis with weights (branches 2.2.1, and 2.3.1 of Fig. 3.3), we generally observe lower sensitivities of the radiogenic heat production of the Upper Crust. For these analyses also the sensitivities of the Mid-German Crystalline High, the Northern Phyllite Zone, and the Rhenohercynian, the Odenwald, and the Alps become negligible.

The results indicate a generally small influence of the radiogenic heat pro-
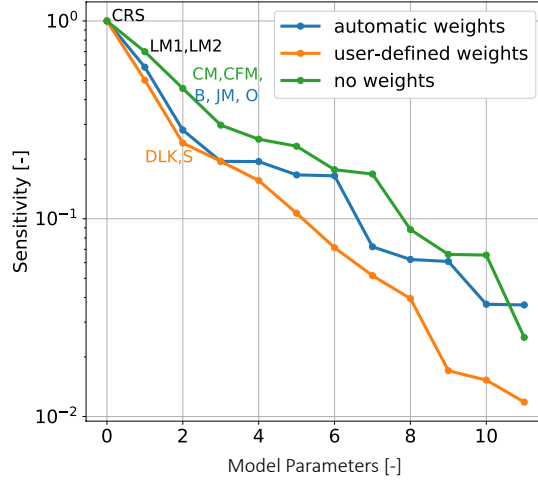
duction, which is subsequently disregarded.

Figure 3.4: Local sensitivity analysis, without weights (green), with user-defined weights (orange), and with automated weights (blue) for the reduced order model varying only the thermal conductivities. The acronyms for the respective geological layers are: CRS = Cenozoic Rift Sediments, CM = Cenozoic Folded Molasse, CFM = Cenozoic Foreland Molasse, DLK = Dogger/Lias/Keuper, B = Buntsandstein, JM = Jura Mountains, S = Saxothuringian, O = Odenwald, LM1 = Lithospheric Mantle 1, and LM2 = Lithospheric Mantle 2.

3.5.2. Model Calibration

The local sensitivity analyses, with a cut-off value of $1 \cdot 10^{-1}$, helped to re-duce the parameter space, such that for the model calibration with user-defined weights (branch 1.3.2 of Fig. 3.3), we have to consider six parameters. The model calibration with automatic weights requires seven parameters (branch 1.2.2 of Fig. 3.3) and the model calibration without weights (branch 1.1.2 of Fig. 3.3) eight parameters instead of twelve. For all weighting versions, we can ignore the Tertiary Salt, the Alps, the Muschelkalk, and the Zechstein/Upper Crust - Alps layers since they are insensitive to the model response. The Cenozoic Volcanics do not need to be considered for the model calibrations with user-defined, and automatic weights. Also, the Malm/Northern Phyllite
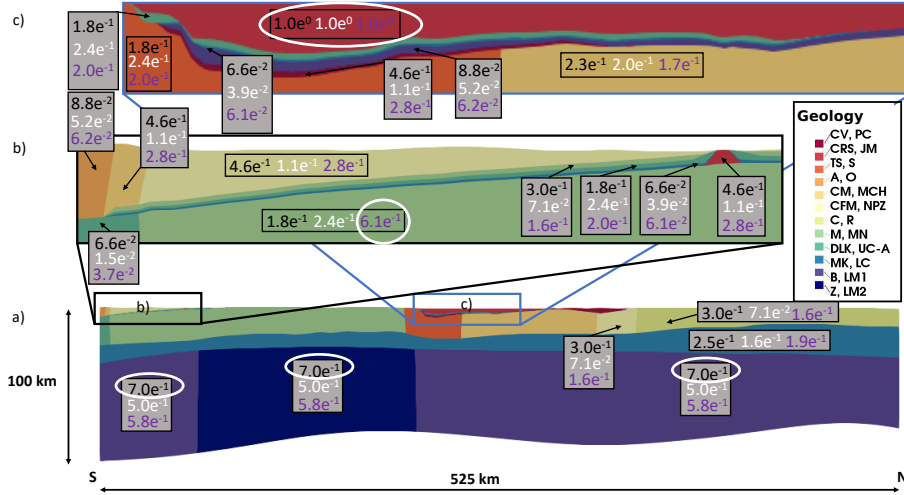
Figure 3.5: We show a cross-section of the Upper Rhine Graben with the local sensitivities of the different geological layers. The position of the cross-section is highlighted by a black line in Fig. 3.1 .The local sensitivities without considering weights are denoted in black, the ones with user-defined weights in white, and the ones with automatic weights in purple. The acronyms for the respective geological layers shown in the color legend are: CV = Cenozoic Volcanics, CRS = Cenozoic Rift Sediments, TS = Tertiary salt, A = Alps, CM = Cenozoic Folded Molasse, CFM = Cenozoic Foreland Molasse, C = Cretaceous, M = Malm, DLK = Dogger/Lias/Keuper, B = Buntsandstein, Z = Zechstein, PC= Permo Carboniferous, JM = Jura Mountains, S = Saxothuringian, O = Odenwald, MCH = Mid-German Crystalline High, NPZ = Nothern Phyllite Zone, R = Rhenohercynian, MN = Moldanubian, UC-A = Upper Crust Alps, LC = Lower Crust, LM1 = Lithospheric Mantle 1, and LM2 = Lithospheric Mantle 2.

Zone/Rhenohercynian are insensitive to the model response for the case of user-defined weights.

The model calibration results for all calibrated thermal conductivities are very similar to those obtained by the model calibration with all parameters (Tab. 2). Only for the Lower Crust and the Lithospheric Mantle, differences are observed. We still, observe that many of the model parameters reach their upper or lower bound.
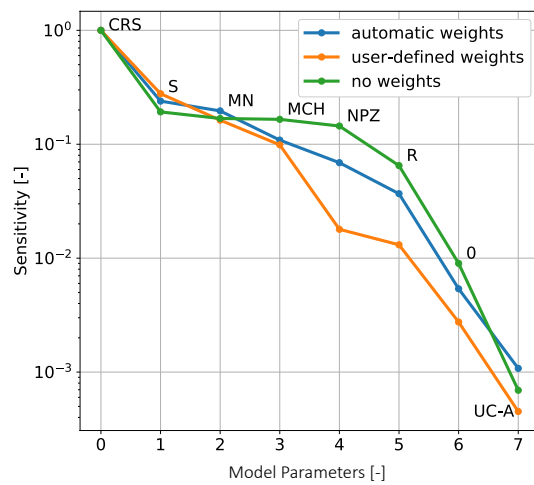
Figure 3.6: Local sensitivity analysis, without weights (green), with user-defined weights (orange), and with automated weights (blue) for the reduced order model varying the thermal conductivity of the Cenozoic Rift Sediments and the radiogenic heat productions of the Upper Crust. The acronyms for the respective geological layers are: CRS = Cenozoic Rift Sediments, S = Saxothuringian, MN = Moldanubian, MCH = Mid-German Crystalline High, NPZ = Nothern Phyllite Zone, R = Rhenohercynian, O = Odenwald, and UC-A = Upper Crust Alps.

Table 2: The thermal properties before and after the calibration for the Upper Rhine Graben with considering the results of the local sensitivity study. The initial thermal properties are taken from Freymark et al. (2017). We denote all parameters that are not involved in the model calibration, due to too low sensitivities, with n/a. Note that UC stands for Upper Crust, ub for upper bound, and lb for lower bound.

ID	Layer	Training Parameter	Initial Bulk Thermal Conductivity [W m^{-1} K^{-1}]	Calibrated Thermal Conductivity [W m^{-1} K^{-1}]			Radiogenic Heat Production [$\mu W m^{-3}$]
				user-defined weights	automatic weights	no weights	
CV	Cenozoic Volcanics	0	1.8	n/a	n/a	2.7 (ub)	0.2
CRS	Cenozoic Rift Sediments	1	1.2	0.8	1.4	1.4	1.0
CM	Cenozoic Folded Molasse	4	3.0	4.5 (ub)	3.3	3.3	1.0
CFM	Cenozoic Foreland Molasse	4	3.0	4.5 (ub)	3.3	3.3	1.0
M	Malm	5	2.7	n/a	2.8 (ub)	2.8 (ub)	1.4

25

DLK	Dogger/Lias-/Keuper	6	2.5	2.4 (lb)	3.2	3.5 (ub)	1.6
B	Buntsand-stein	4	3.0	4.5 (ub)	3.3	3.3	1.0
JM	Jura Mountains	4	3.0	4.5 (ub)	3.3	3.3	0.5
S	UC: Saxo-thuringian	6	2.5	2.4 (lb)	3.2	3.5 (ub)	2.5
O	UC: Oden-wald	4	3.0	4.5 (ub)	3.3	3.3	1.8
MCH	UC: Mid-German Crystalline High	9	2.4	2.7 (ub)	2.3 (lb)	2.3 (lb)	1.8
NPZ	UC: Nothern Phyllite Zone	5	2.7	n/a	2.8 (ub)	2.8 (ub)	3.0
R	UC: Rheno-hercynian	5	2.7	n/a	2.8 (ub)	2.8 (ub)	1.0
MN	UC: Moldanubian	6	2.5	2.4 (lb)	3.2	3.5 (ub)	2.6
LC	Lower Crust	10	2.1	2.1 (lb)	2.6	2.1 (lb)	0.5
LM1	Lithospheric Mantle 1	11	3.95	4.3	5.9 (ub)	5.9 (ub)	0.03
LM2	Lithospheric Mantle 2	11	3.95	4.3	5.9 (ub)	5.9 (ub)	0.03

3.6. Model Calibration with Global Sensitivity Analysis

In the following, we present the results from the global sensitivity study and the model calibration using these sensitivity results. Again, we perform all analyses for the scenarios: i) no weights, ii) automatic weights, iii) user-defined weights.

3.6.1. Sensitivity Analysis

At first, we consider the reduced model with varying thermal conductivities and the scenario without weights (branch 1.1.3 of Fig. 3.3). The Sobol sensitivity analysis (Fig. 3.7, 3.8) shows that the Cenozoic Rift Sediments dominantly influence the model. In addition to the sensitivities for each parameter, we now also obtain an indication of higher-order contributions (see Section 2.1.2), which can be attributed to parameter correlations. The major part of the sensitivity is first-order, and only a minor part is originating from higher-order contributions. The second highest sensitivity is coming from the Cenozoic Volcanics and also has dominantly first-order contributions. Note that the third highest sensitivity is arising from the thermal conductivity of the Lithospheric Mantle, which has mainly higher-order contributions. Also, the Cenozoic Folded Molasse/Cenozoic Foreland Molasse/Buntsandstein/Jura Mountains/Odenwald layers are minorly influencing the model with predominantly first-order contributions. The influences from all remaining layers are negligible with values of less than $1 \cdot 10^{-2}$.

The Sobol sensitivity analysis for the same reduced model with user-defined weights (branch 1.3.3 of Fig. 3.3) results in a slightly different pattern. For this scenario, the model is still predominately influenced by the Cenozoic Rift Sediments, but it has nearly no higher-order contributions. Furthermore, the Lithospheric Mantle influence the model significantly. Again, the first-order contributions are dominant and the higher-order contributions are nearly non-existent. The influences from the Cenozoic Volcanics and the Cenozoic Folded Molasse/Cenozoic Foreland Molasse/Buntsandstein/Jura Mountains/Odenwald layers are no longer observable. The Sobol sensitivity analysis with automatic weight (branch 1.2.3 of Fig. 3.3) yields nearly the same results as the analysis

27

without weights. The analyses took in total 260,000 function evaluations each yielding an execution time of under 500 s.

Furthermore, we performed a Sobol sensitivity analysis (with and without weights) with eight parameters (branches 2.1.2, 2.2.2, and 2.3.2 of Fig.3.3, and Fig. 3.9): the thermal conductivity of the Cenozoic Rift Sediments and the radiogenic heat production rates of the Upper Crust. From all radiogenic heat productions, only the one from the Saxothuringian influences the model for both the analysis with and without weights. However, the influence is minimal in comparison to the thermal conductivity of the Cenozoic Rift Sediments. Higher-order contributions dominate the radiogenic heat production of the Saxothuringian, for the analysis without weights (branch 2.1.2 of Fig. 3.3). Similar to the sensitivity analysis using the first reduced model, we observe a drastic increase in the first-order contributions for the analysis with user-defined weights (branch 2.3.2 of Fig. 3.3). Again, for the analysis with automatic weights (branch 2.2.2 of Fig. 3.3), we get the same results as for the analysis without weights. For each of these analyses, we need 180,000 function evaluations, and less than 90 s compute time.

3.6.2. Model Calibration

For the calibration, we now consider only the thermal conductivities (branches 1.1.3, 1.2.3, and 1.3.3 of Fig. 3.3) since the Sobol sensitivity analysis showed that the influence of the radiogenic heat production is small in comparison to the thermal conductivity. As before, we repeat the calibration in three scenarios. In the "no weight", and "automatic weight" scenario (branches 1.1.3, and 1.2.3 of Fig. 3.3), we calibrate with only four instead of 12 parameters. These four parameters are the thermal conductivities of the:

- Cenozoic Volcanics

- Cenozoic Rift Sediments

- Cenozoic Forleand Molasse, Buntsandstein, Jura Mountains, Odenwald
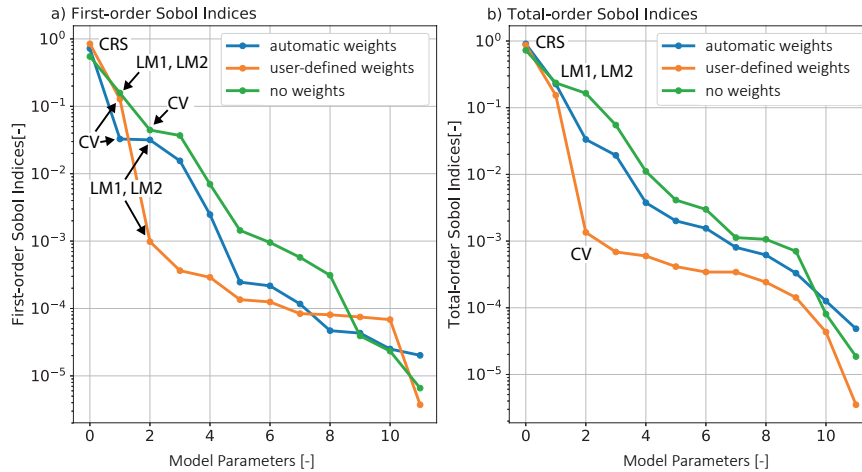
- Lithospheric Mantle

Figure 3.7: Global sensitivity analysis, without weights (green), with user-defined weights (orange), and with automated weights (blue) for the reduced order model varying only the thermal conductivities. The acronyms for the respective geological layers are: CRS = Cenozoic Rift Sediments, CV= Cenozoic Volcanics, LM1 = Lithospheric Mantle 1, and LM2 = Lithospheric Mantle 2.

The global sensitivity analysis revealed that the model is insensitive to the other eight parameters. For the case with user-defined weights (branch 1.3.3 of Fig. 3.3), we consider only two parameters. The calibrations require at most seven function evaluations, resulting in a computation time of under 100 ms.

We observe the highest misfit for the temperatures of the initial parameter distribution and the parameter distribution after the calibration without weights (branch 1.1.3 of Fig. 3.3) in the southern and central part of the Upper Rhine Graben (Fig. 3.10). Focusing on the area of the highest misfit, we observe in the central part of this area underestimated temperature values yielding a temperature misfit of -10 °C to -40 °C. In the southern and northern part, we observe overestimated and underestimated temperature values ranging from -20 °C to 70 °C.

For the parameter distribution after the calibration with user-defined weights (branch 1.3.3 of Fig. 3.3), we see a similar pattern. Note that the underestimation of the temperature in the central part of the misfit area increased. This
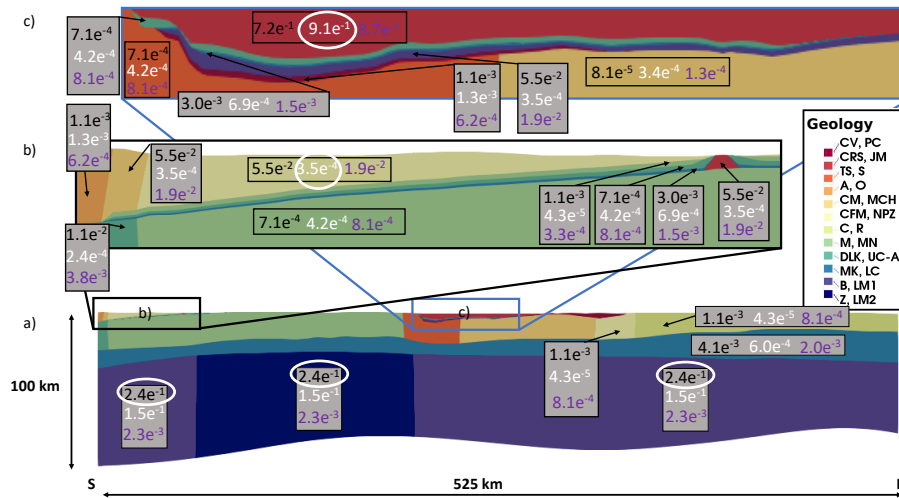
Figure 3.8: Cross-section of the Upper Rhine Graben with the global sensitivities of the different geological layers. The global sensitivities without considering weights are denoted in black, the ones with user-defined weights in white, and the ones with automatic weights in purple. The acronyms for the respective geological layers shown in the color legend are: CV = Cenozoic Volcanics, CRS = Cenozoic Rift Sediments, TS = Tertiary salt, A = Alps, CM = Cenozoic Folded Molasse, CFM = Cenozoic Foreland Molasse, C = Cretaceous, M = Malm, DLK = Dogger/Lias/Keuper, B = Buntsandstein, Z = Zechstein, PC= Permo Carboniferous, JM = Jura Mountains, S = Saxothuringian, O = Odenwald, MCH = Mid-German Crystalline High, NPZ = Nothern Phyllite Zone, R = Rhenohercynian, MN = Moldanubian, UC-A = Upper Crust Alps, LC = Lower Crust, LM1 = Lithospheric Mantle 1, and LM2 = Lithospheric Mantle 2.

results in a temperature misfit of around -70 °C. In contrast, the overestimation in the southern and northern part decreased, yielding temperature differences of around 10 °C to 50 °C. This is the main reason why the average misfit in region 2 (located in the southern and central part of the Upper Rhine Graben) decreased from 29 °C to 17 °C. The misfit distribution for the parameters after the calibration with automatic weights (branch 1.2.3 of Fig. 3.3) is similar to the one without weights.

The initial temperature distribution in the overall model of the Upper Rhine Graben varies from -1 °C to 1300 °C. At the upper part of the model, we observe
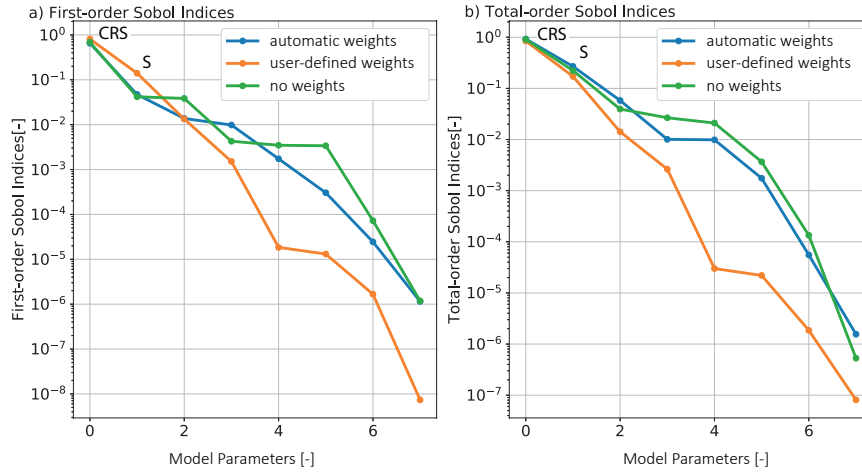
Figure 3.9: Global sensitivity analysis, without weights (green), with user-defined weights (orange), and with automated weights (blue) for the reduced order model varying the thermal conductivity of the Cenozoic Rift Sediments and the radiogenic heat productions of the Upper Crust. The acronyms for the respective geological layers are: CRS = Cenozoic Rift Sediments, and S = Saxothuringian.

much steeper thermal gradients than in the lower part of the model. The misfit between observed and simulated temperatures has its highest values in the area of the Upper Rhine Graben. Within the Upper Rhine Graben the highest misfits are in regions 2 and 3.

We now focus on the calibrated thermal conductivities (Tab. 3). Regarding the calibration without weights (branch 1.1.3 of Fig. 3.3, and Fig. 3.11), we observe, for the Cenozoic Volcanics and Rift Sediments and the Lithospheric Mantle, an increase in thermal conductivity in contrast to the initial thermal conductivities. This yields thermal conductivities of 2.4 W m^{-1} K^{-1}, 1.3 W m^{-1} K^{-1}, and 4.9 W m^{-1} K^{-1}, respectively. The Cenozoic Folded Molasse/Cenozoic Foreland Molasse/Buntsandstein/Jura Mountains/Odenwald layers have with a thermal conductivity of 3.0 W m^{-1} K^{-1}, the same value before and after the calibration. The calibration with automatic weights (branch 1.2.3 of Fig. 3.3) yields similar thermal conductivities as the one without weights.

For the calibration with user-defined weights (branch 1.3.3 of Fig. 3.3, Fig.
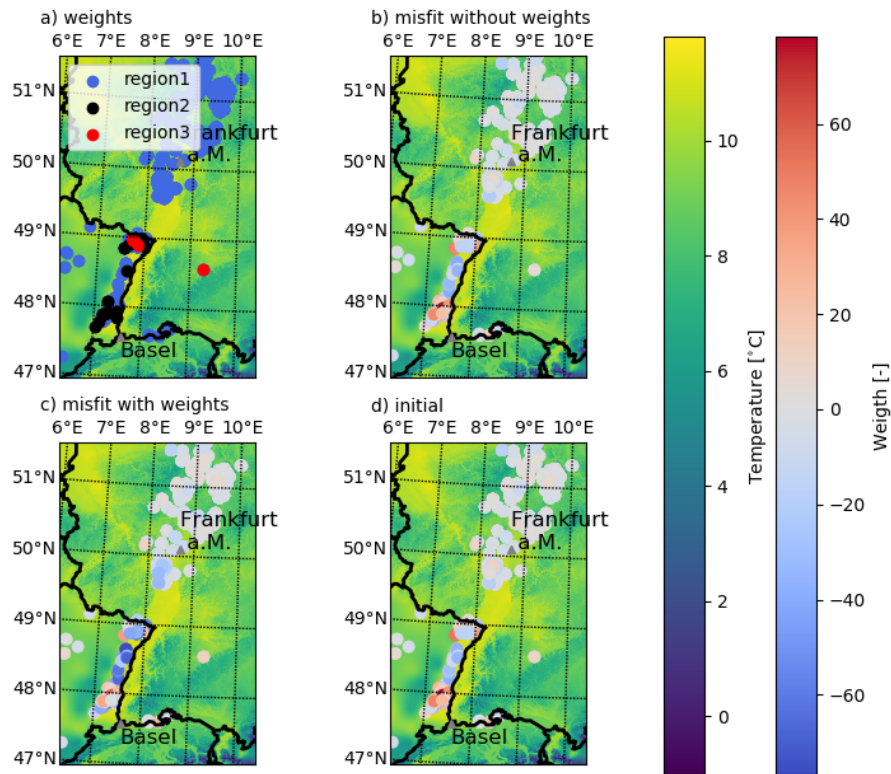
Figure 3.10: Spatial distribution of a) the user-defined weights b) the misfit in temperature for the calibration without weights c) the misfit in temperature after the calibration with user-defined weights, and d) the misfit in temperature for the initial parameter distribution. In the background of all images are the annual regional average surface temperature values plotted to outline the region of the Upper Rhine Graben.

3.12), we observe for the Rift Sediments a decrease in thermal conductivity after the calibration, resulting in an extremely low thermal conductivity of 0.8 W m^{-1} K^{-1}. The Lithospheric Mantle has a slightly decreased thermal conductivity of 3.6 W m^{-1} K^{-1} in contrast to the initial thermal conductivity of 3.95 W m^{-1} K^{-1}.

Table 3: The thermal properties before and after the calibration for the Upper Rhine Graben considering the results of the global sensitivity study. The initial thermal properties are taken from Freymark et al. (2017). We denote all parameters that are not involved in the model calibration, due to too low sensitivities, with n/a. Note that UC stands for Upper Crust.

ID	Layer	Training Parameter	Initial Bulk Thermal Conductivity [W m^{-1} K^{-1}]	Calibrated Thermal Conductivity [W m^{-1} K^{-1}]			Radiogenic Heat Production [$\mu W m^{-3}$]
				user-defined weights	automatic weights	no weights	
CV	Cenozoic Volcanics	0	1.8	n/a	2.6	2.4	0.2
CRS	Cenozoic Rift Sediments	1	1.2	0.8	1.3	1.3	1.0
CM	Cenozoic Folded Molasse	4	3.0	n/a	2.9	3.0	1.0
CFM	Cenozoic Foreland Molasse	4	3.0	n/a	2.9	3.0	1.0
B	Buntsandstein	4	3.0	n/a	2.9	3.0	1.0

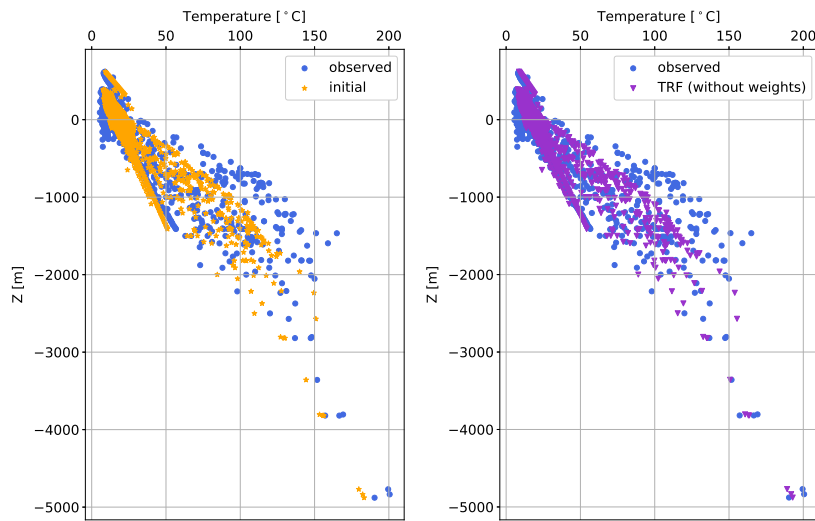| JM	Jura Mountains	4	3.0	n/a	2.9	3.0	0.5
O	UC: Odenwald	4	3.0	n/a	2.9	3.0	1.8
LM1	Lithospheric Mantle 1	11	3.95	3.6	5.2	4.9	0.03
LM2	Lithospheric Mantle 2	11	3.95	3.6	5.2	4.9	0.03

Figure 3.11: On the left side, the temperature distribution of the observed data and the initial parameter distribution are shown. The right image shows the observed data and the temperature distribution of the parameters after the trust region reflection (TRF) calibration without weights.
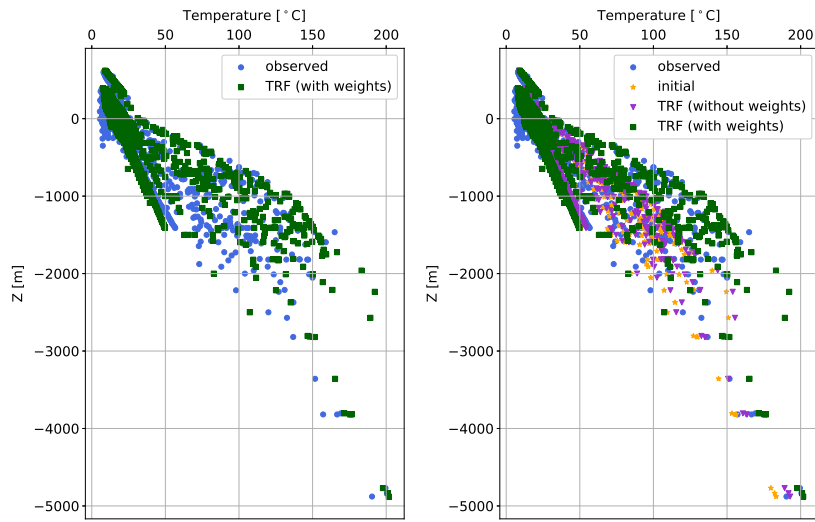
Figure 3.12: On the left side, the observed data and the temperature distribution after the trust region reflective (TRF) calibration with user-defined weights are shown. The right image shows the temperature distribution of the observed data, the initial parameter distribution, and the parameter distribution after the calibration with and without weights. Only for the temperature distribution after the calibration with user-defined weights, we find a good agreement of the temperature values for all parts of the model.

3.7. Computational Cost

Table 4: Overview of the computational costs for both reduced models of the Upper Rhine Graben.

Model	FE simulation time [s]	Number of basis functions	Online time [s]	Speed-up
1. RB model	2,640	128	0.003	$9.2 \cdot 10^5$
2. RB model	2,640	25	0.001	$2.7 \cdot 10^6$

The reduction requires 128 basis functions to describe the model for a relative error tolerance of $5 \cdot 10^{-4}$ for the Upper Rhine Graben model, where we vary only the thermal conductivities (Tab. 4, branch 1 of Fig. 3.3, and Fig. 3.13). We can reduce the compute time of a single forward simulation from 44 min to 3 ms, yielding a speed-up of $9.2 \cdot 10^5$. For the model with a varying thermal conductivity of the Cenozoic Rift Sediments and the varying radiogenic heat productions of the Upper Crust (Tab. 4, branch 2 of Fig. 3.3), 25 basis functions are required to reach an error tolerance of $1 \cdot 10^{-5}$. Here, we reduce the computation time to 1 ms, resulting in a speed-up of $2.7 \cdot 10^6$.

4. Discussion

The results of our case studies highlight that global sensitivity analyses are essential for meaningful, comprehensive, and robust geothermal model calibrations. This aspect is specifically relevant in comparison to a "trial-and-error" model calibration. In the following, we will discuss these findings in more detail, in addition to a discussion of the computational cost of using the RB method instead of the classical FE method.

4.1. Sensitivity Analysis

The global sensitivity analysis without weights (branch 1.1.3 of Fig. 3.3) indicated that the model is dominated by first-order contributions from the
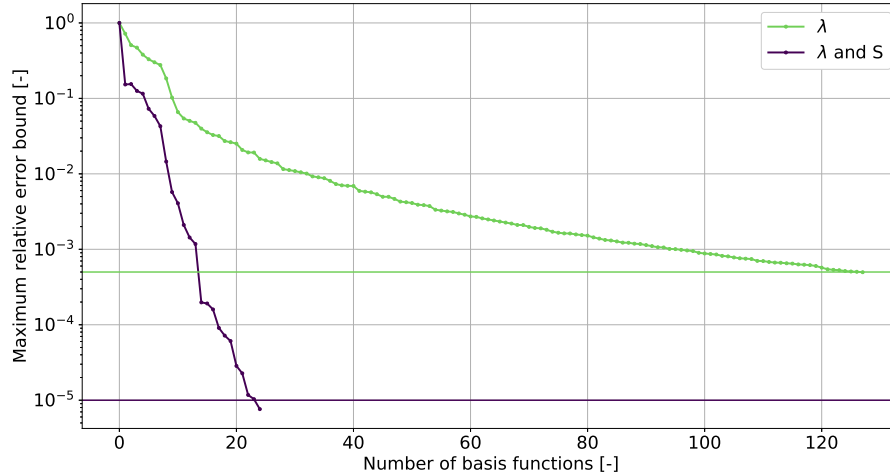
Figure 3.13: Convergence of the relative maximum error bound for both reduced order models. The error bound is relative to the approximation of the "truth" (FE solution). For that reason, it is a measure of the approximation quality.

thermal conductivity of the Cenozoic Rift Sediments. Hence, the highest influence from that layer is coming from the layer itself and not from correlations with other layers.

The model, is to a lesser degree, influenced by the thermal conductivities of the Cenozoic Volcanics and the Lithospheric mantle. They both have similar total sensitivities, the thermal conductivity of the Cenozoic Volcanics has mostly influences arising from the parameter itself and nearly no influences originating from the correlation with other parameters. This might lead to the conclusion that for this specific model, a local sensitivity analysis would be sufficient.

Furthermore, with the measurements located in the upper layers (deepest measurement at about 7 km depth), it is expected that the model is mostly influenced by the upper layers.

This is however not the case because:

1. We have shown that already for the simplified basin-scale model, even if nearly no correlation is observed, the local sensitivity analysis overesti-

mates the influence of the model parameters on the model response (see Fig. 2.2).

2. The thermal conductivity of the Lithospheric mantle, on the other hand, has nearly only influences arising from correlations to other parameters, which is only visible through performing a global sensitivity analysis.

3. In case of the local sensitivity analysis, we need to assume a reference parameter set, which is highly dependent on our prior knowledge.

The smaller influence from the Cenozoic Volcanics is caused by the upper boundary condition. At the top of the model, we applied a Dirichlet Boundary condition, which fixes the temperatures to the regional average annual temperature values. Hence, the possible model variations in the uppermost part of the model are limited and therefore also the sensitivities are smaller. The high influence from the Lithospheric mantle is caused by the large layer thickness. The model is furthermore to a lesser degree influenced by the thermal conductivity of the Cenozoic Folded Molasse/Cenozoic Foreland Molasse/Buntsandstein/Jura Mountains/Odenwald layers. For the global sensitivity analysis, with weights (branch 1.3.3 of Fig. 3.3), we observed that the sensitivity towards the thermal conductivities of the Cenozoic Volcanics and Cenozoic Folded Molasse/Cenozoic Foreland Molasse/Buntsandstein/Jura Mountains/Odenwald layers are vanishing. Furthermore, the first-order contributions are drastically increasing with respect to the other global sensitivity studies (branches 1.1.3, and 1.2.3 of Fig. 3.3), which further emphasizes that the model is mainly influenced by the thermal conductivities of the layers themselves and not through the correlation with other thermal conductivities.

If we compare the results with the local sensitivity studies (branches 1.1.2, 1.2.2, and 1.3.2 of Fig. 3.3), we observe that the local study is overestimating the influence of the remaining layers. Furthermore, we cannot distinguish between first- and higher-order contributions. Therefore, it is not possible to investigate the correlation between the parameters.

The influences of the radiogenic heat production are negligible in comparison

to the thermal conductivities. This is the reason why we did not account for these parameters in further analyses. The minor influence of the radiogenic heat production is contradictory to the results from Freymark et al. (2017). The discrepancy is either caused by the choice of the sensitivity analysis (we used a global study in contrast to the local study from Freymark et al. (2017)), or different quantities of interests.

4.2. Model Calibration

We investigate the robustness of the model calibrations without weights and with user-defined weights (branches 1.1.1 to 1.1.3, to 1.3.1 to 1.3.3 of Fig. 3.3) by decreasing the allowed variation range from $\pm$ 50 % to $\pm$ 10 % in step sizes of 10 %. For this analysis, only the model calibration with a global sensitivity analysis behaves in accordance with our expectations. Both the model calibration without a sensitivity study and with a local sensitivity study behave nonphysically. As an example, if we define a variation range of $\pm$ 10 % the thermal conductivity of the Cenozoic Folded Molasse/Cenozoic Foreland Molasse/Buntsandstein/Jura Mountains/Odenwald layers decreases to its lower bound of 2.7 W m^{-1} K^{-1}. Note that the initial value is 3.0 W m^{-1} K^{-1}. However, if we now increase the variation range to $\pm$ 20 %, then the thermal conductivity increases to its upper bound of 3.6 W m^{-1} K^{-1}, which is physically not plausible.

In order to control the robustness of the different model calibration versions, we performed the model calibration without a sensitivity study, with a local sensitivity study, and with a global sensitivity study with different initial guesses. All model calibrations were tested using the user-defined weights (branches 1.3.1 to 1.3.3 of Fig. 3.3). We tested the parameter values provided by Freymark et al. (2017) as initial guess, the lower and upper parameter bounds, and ten randomly chosen initial parameter sets. The least robust model calibration is the one without a sensitivity analysis (branch 1.3.1 of Fig. 3.3). It shows the highest differences with thermal conductivity differences in the order of 10^{-2} W m^{-1} K^{-1}.
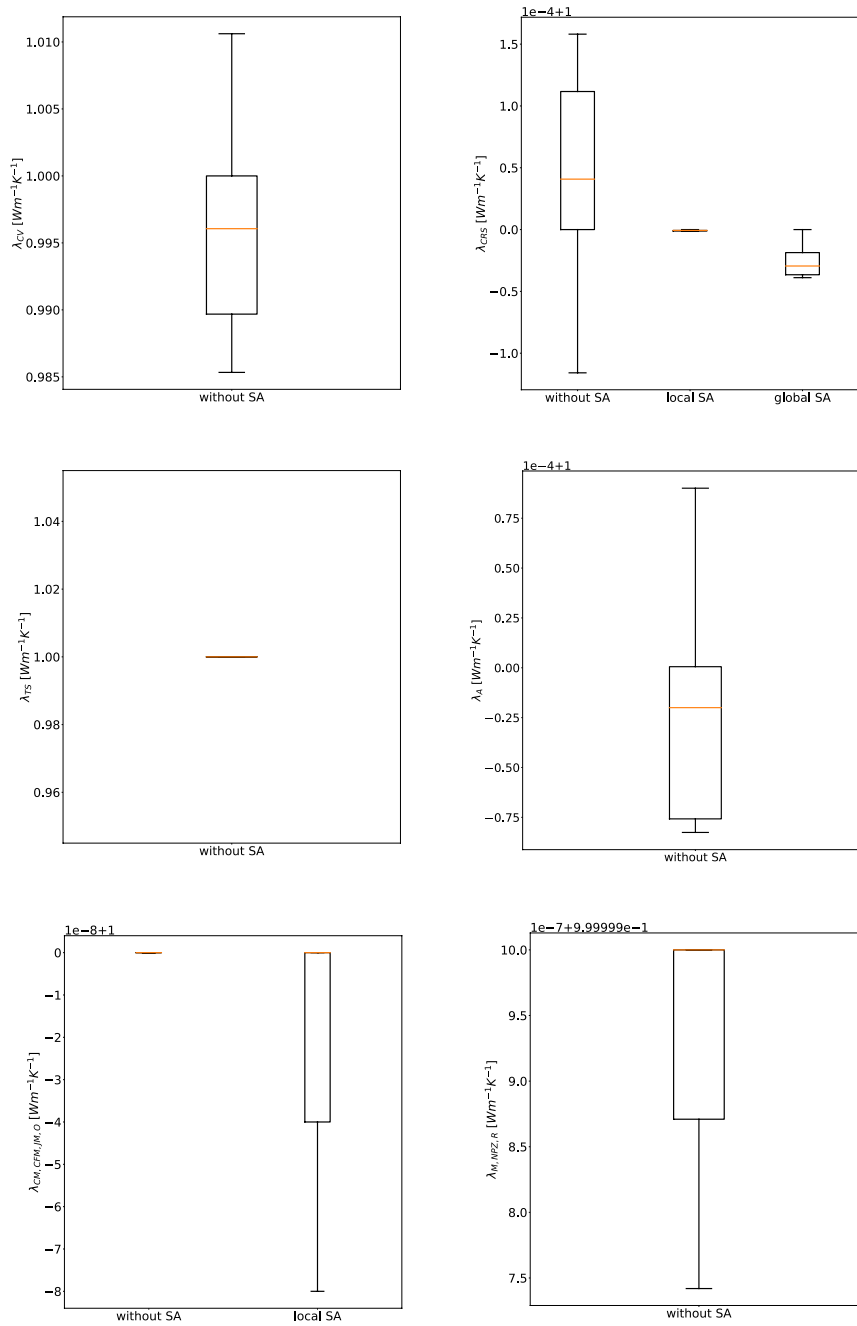
Figure 4.1: Box plot for all thermal conductivities of the Upper Rhine Graben. The median is denoted in orange. All thermal conductivities are normalized by the calibration results using the parameter values from (Freymark et al., 2017) to better visualize the differences. The acronyms for the respective geological layers are defined in Tab. 1.
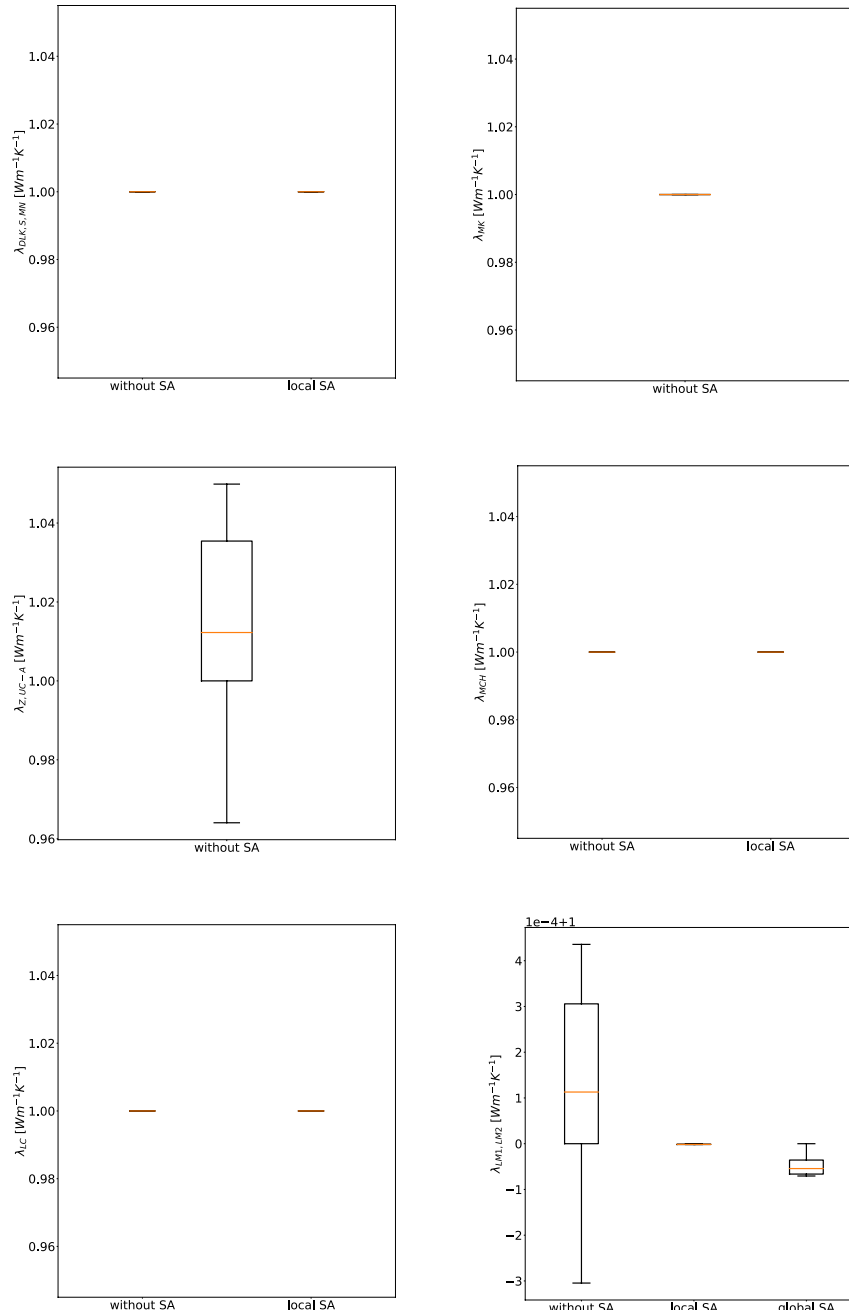
40

Figure 4.2: Continuation: Box plot for all thermal conductivities of the Upper Rhine Graben. The median is denoted in orange. All thermal conductivities are normalized by the calibration results using the parameter values from (Freymark et al., 2017) to better visualize the differences. The acronyms for the respective geological layers are defined in Tab. 1.

41

The model calibration with a local sensitivity analysis (branch 1.3.2 of Fig. 3.3) yields differences in the order of 10^{-5} W m^{-1} K^{-1}, and the one with a global sensitivity (branch 1.3.3 of Fig. 3.3) difference in the order of 10^{-4} W m^{-1} K^{-1}. Hence, a first conclusion might be that both the model calibrations with the local and the global sensitivity study result in robust model calibrations since they converge to the same results.

However, if we look a bit closer at the model calibration with the local sensitivity study this impression is lost. Those parameters that reach the bounds show, as displayed in Fig. 4.1, and Fig. 4.2, in most realizations a difference for the parameter values of exactly zero with respect to the initial parameter set of Freymark et al. (2017). That is extremely suspicious since at least differences caused by numerical errors should be visible. This leads to the conclusion that the model calibration with the local sensitivity study is robust for the model parameters that do not reach their bounds and stuck for those that reach one of their bounds. So, overall it is a non-robust model calibration.

Many of the calibrated parameter values of the model calibrations without a sensitivity study and with a local sensitivity study yield unphysical parameter values. In contrast, if we look at the model calibration using a global sensitivity study we see that independent on the weighting, no calibrated parameter reaches its bound (Tab. 3). However, the cost of the sensitivity-driven model calibration is extremely high because of the global sensitivity analysis. So, why can we not use a local sensitivity study? The reasons become apparent if we look at the results of the model calibration using a local sensitivity analysis (Tab. 2). The calibrated parameter values are nearly identical to the ones without a sensitivity study (Tab. 1). We are able to reduce the number of parameters from twelve to six, seven, or eight parameters depending on the weighting. Nonetheless, many parameters are still reaching their pre-defined bounds. This either shows that:

- the bounds were not placed far enough away from the initial parameter distribution

- or that the parameters are insensitive to the temperature distribution and

the results, therefore, meaningless.

This is potentially problematic. Considering, the already quite large variation range (up to $\pm$ 50 %), it is more likely that the parameters that reach their bounds are insensitive to the model response. In case of insensitive parameters, the model calibration will fail to correctly determine the parameter values since all possible parameter values result in the same temperature distribution. If we still have insensitive parameters after performing a local sensitivity study this consequently means that the local sensitivity study fails to successfully reduce the parameter space, assuming well defined bounds. This yields two major problems:

1. In case we want to perform predictions away from known observations, we obtain possible biased and overfitted results.
2. We used the sensitivity-driven model calibrations for identifying model areas, where the current model insufficiently describes the temperature distribution. That would no longer be possible since the drastic change in the parameter values would misleadingly indicate a model error.

This, in combination with the non-robustness of both model calibrations, leaves only the model calibration with a global sensitivity study as a robust and reliable model calibration.

We are not only able to identify the most influencing parameters but also to investigate to which degree the individual parameters are correlated with each other. Furthermore, the automated calibration is a systematic way to explore the entire parameter space. A "trial-and-error" model calibration allows to compute a handful of realizations but it is far away from giving a guarantee to find the optimal parameter set. Additionally, it will not consider any correlations with other parameters and will result in more qualitative than quantitative results, and is usually not reproducible. An automated model calibration is reproducible, something that is not true for the "trial-and-error" model calibration. Within this paper, we perform model calibrations with and without weights.

Using the model calibration with user-defined weights and a global sensitivity analysis (branch 1.3.3 of Fig. 3.3) leaves us with two parameters that can be calibrated: the Cenozoic Rift Sediments, and the Lithospheric mantle. This is in accordance with our geological understanding of the model. In case of the user-defined weights, we concentrate the calibration nearly exclusively on the area of the Upper Rhine Graben, in order to explain the mismatch of the temperature values in region 2 from the initial parameter distribution. If we, however, focus our analysis on the Upper Rhine Graben itself, the calibration will be dominated by the dominant geological layer of the Upper Rhine Graben: the Cenozoic Rift Sediments. Only, the global sensitivity analysis is able to represent our geological understanding of the model. Note, that if we focus the model calibration on the entire model we can also determine the behavior of other layers such as the Cenozoic Volcanics.

For all model calibrations, we observe, inside the Upper Rhine Graben, two regions of over-fitted temperature values and one region of under-fitted temperature values. The boundary of this region correlates with the vertical boundaries of the variscan units.

This indicates a possibly wrong geometrical model, whose improvement is subject to future studies.

Using a sensitivity-driven automated model calibration instead of a "trial-and-error" model calibration, as done in the previous studies, has several advantages:

1. Through the sensitivity analysis, it is possible to identify the parameters that do not influence the model and hence to reduce the number of parameters that have to be considered in further analyses, which reduces the computational cost.

2. A global sensitivity study, as the Sobol analysis, has further the advantage that it provides both first-order and higher-order sensitivities and, therefore, an additional insight into the model structure.

This further emphasizes the need for global sensitivity studies since, indepen-

dent of how correlated the individual parameters are, the local sensitivity study fails to reduce the parameter space due to the overestimation of the sensitivities of the model parameters.

The reliance on the reference parameters could be addressed by using a Morris sensitivity analysis (Campolongo et al., 2007; Morris, 1991; Wainwright et al., 2014). The Morrison sensitivity analysis is, as the local sensitivity analysis, difference-based. It requires usually less forward simulations than the Sobol sensitivity analysis and is, therefore, computationally cheaper. In contrast to the Sobol sensitivity analysis, it does not allow an intensive study of the parameter correlations (Campolongo et al., 2007; Morris, 1991; Wainwright et al., 2014). Since these correlations are of major interest in geothermal studies, we advise using the Sobol sensitivity analysis with a surrogate model to compensate for the computational costs.

Regarding the thermal conductivities, we observe a significant decrease in thermal conductivity in the upper two layers for the model calibrations with user-defined weights (branch 1.3 of Fig. 3.3). No changes are observed for the Cenozoic Folded Molasse/Cenozoic Foreland Molasse/Buntsandstein/Jura Mountains/Odenwald layer and only a slight decrease in the Lithospheric mantle. This demonstrates that except for the Cenozoic Volcanics and Rift Sediment layer a conductive model is sufficient to describe the temperature distribution of the Upper Rhine Graben, this is also in accordance with previous studies (for instance Freymark et al. (2017)). However, it also demonstrates that the model is, in its current form insufficient to describe the temperature distribution arising from the upper two layers. That is not seen in the model calibration without weights because of the above-described reasons.

4.2.1. On the Validity of the Physical Model

The spatial distribution of the misfit suggests that a conductive model is sufficient to describe the temperature distribution in the area outside the southern and central part of the Upper Rhine Graben. In the mentioned area, we observe a significant misfit to the observed temperatures. The calibration with weights

shows that this misfit is caused by an effect that leads to a decreased thermal conductivity in the Cenozoic Volcanics and Rift Sediments. By having a closer look at this area in the literature we find that especially the area of the central part of the Upper Rhine Graben is characterized by highly permeable sediments with a dense fault network (Buchmann & Connolly, 2007; Bauer et al., 2015; Vidal & Genter, 2018; Meixner et al., 2016). Combining these structural characteristics, and the discrepancy in the thermal conductivity of the upper two layers, we can conclude that the misfit might be related to fluid interactions and related effects on heat transport, which are not considered in the conductive model. In Fig. 4.3, we show the results of a hydrothermal simulation for the Upper Rhine Graben. The blue arrows show how the fluid movement is influenced by the two border faults. This flow pattern leads to an increased heat transfer inside the graben. Due to the no flow conditions at the vertical model boundaries, the amount of heat in the Cenozoic Rift Sediments increases resulting in the extremely low "effective" thermal conductivity.

In contrast to previous studies, we are able to identify the two layers that are responsible for the misfit and systematically determine which of these layers is of higher importance. Furthermore, based on the sensitivity analysis, we can determine that most of these misfits are caused by the two layers themselves and only a significantly smaller part is introduced by the correlation with other parameters.

4.2.2. On the Scenarios with Different Weighting Schemes

One main difficulty arising from the observation data is the very uneven spatial distribution. We have 2282 data points in region 1, 53 in region 2 and 12 data points in region 3 (Fig. 3.10). Hence, region 1 contains one order of magnitude more data than region 2 and two orders of magnitude more data than region 3. Performing a calibration without applying any weights to the data will, therefore, reduce the misfit in region 1 but only to a limited amount the misfits in regions 2 and 3 since the contribution of the misfit of these regions to the overall misfit is very small. This can clearly be seen in Fig. 3.10 by
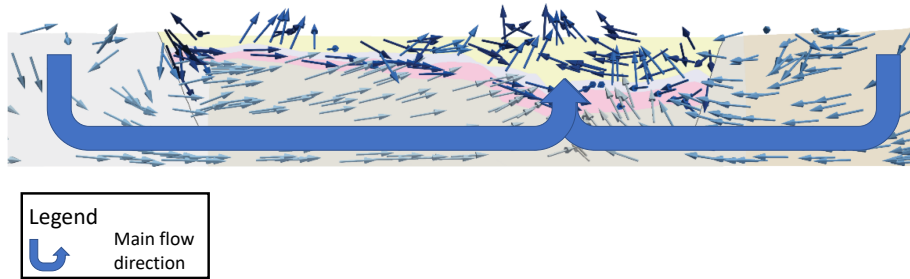
Figure 4.3: Representation of the fluid flow in the Upper Rhine Graben that explains the lower effective thermal conductivity for the Cenozoic Rift Sediments (modified after Freymark et al. (2019)).

comparing the temperature values of the model calibration without weights and the initial temperature distribution because the difference between these two is insignificant especially under consideration of the measurement accuracy. If we are only interested in region 1 of the model it is sufficient to follow the approach of a model calibration without any weights. If we are, however, interested in a more even fit over the entire spatial domain of the model, this is not enough. In order to compensate for the unequal distribution of observations, we apply user-defined weights to the different regions as described in Section 3.2. This results in a slightly worse fit for region 1 compared to the initial temperature distribution. However, the misfit in region 2 can be decreased from 29 °C to 17 °C. The misfit in region 3 is comparable for both realizations.

The question arises why the calibration with automatic weights yields very similar results to the calibration without weights. This can be explained by having a closer look at the spatial distribution of the misfit inside the southern and central part of the Upper Rhine Graben. In there, we can identify three regions: i) in the central part a region of overall underestimated temperatures and ii) north and south to it regions of overall overestimated temperatures. These regions of over- and underestimated temperatures correspond to region 2 and are therefore the region in which the conductive model fails to represent the measured temperature distribution. If we use the automated weighting scheme

that considers distances only, we apply a higher weight to both the over- and underestimated temperature regions. The model calibration method minimizes the total misfit. By applying now a higher weight to both the over- and underestimated temperature regions in the Upper Rhine Graben we increase for both parts the contribution to the total misfit. However, only the overestimated temperatures correspond to region 2. Hence, if we only apply a higher weight to the overestimated temperature region, as done in the weighting scheme based on expert knowledge, we increase the contribution to the total misfit of this region alone. In comparison to the others, we obtain a model that is spatially more balanced.

4.3. Computational Cost

Table 5: Overview of the computational costs for the sensitivity analysis of both reduced models of the Upper Rhine Graben.

Model	FE simulation time [min]	Offline Stage [h]	Number of basis functions	Online time [s]	Speed-up	Global SA [s]	Local SA [s]
1. RB model	$2.64 \cdot 10^3$	$1.27 \cdot 10^5$	128	$3 \cdot 10^{-3}$	$9.2 \cdot 10^5$	$5 \cdot 10^2$	$5 \cdot 10^{-2}$
2. RB model	$2.64 \cdot 10^3$	$8.39 \cdot 10^4$	25	$1 \cdot 10^{-3}$	$2.7 \cdot 10^6$	$9 \cdot 10^1$	$1 \cdot 10^2$

Generating the RB model has an initial computational cost, which is represented by the compute time of the offline stage (Tab. 5). The offline stage of the Upper Rhine Graben with varying thermal conductivities required 128 basis functions and took 35.7 h, on an Intel Westmere X675 machine (3.07 GHz 6 cores per chip, 12 cores per node and 24 GB memory per node) using 48 cores. The other offline stage, with varying radiogenic heat productions required 25

basis functions yielding a total compute time of 23.3 h on the same machine. If we compare that to the total number of function evaluations of around 440,000, it becomes obvious that we are far more efficient with the reduced basis method than with the finite element method. Furthermore, the reduction is a one-time cost. So, we can use the same reduced model for further investigations and do not require another time-consuming offline stage.

In the current stage, the RB method provides error bounds only for elliptic and parabolic partial differential equations (PDE). For geothermal applications, this has the consequence that the method is only applicable to conductive studies. Also note, that we need to decompose the PDE into a parameter-dependent and -independent part. This is naturally given for linear problems, but not for nonlinear ones. Nonetheless, the method is also applicable for nonlinear PDEs by using the empirical interpolation method (e.g. Barrault et al., 2004), which approximates the nonlinear part of the PDE.

4.4. Outlook

This study opens up the path to several subsequent steps. It would be interesting for further studies to incorporate geometric uncertainties from the structural model, and to repeat the model calibration process in order to investigate the influence of these uncertainties on the model. Furthermore, it would be interesting to investigate the changes in the conductive temperature distribution by improving the geometrical parameterization of the Varisican units. The calibration indicated that we need to consider the fluid interaction in the upper layers. Due to the high dimensionality of the model, a hydrothermal simulation becomes computationally very costly, making global sensitivity analyses as investigated here prohibitively expensive. Furthermore, the number of parameters that need to be calibrated increases, making a calibration of the individual parameters increasingly difficult, due to the data sparsity (Freymark et al., 2019). In order to perform both efficient inverse processes and consider the hydrothermal effects, we want to use concepts, as the entropy production (Börsing et al., 2017), to transfer the effects of the convection into effective thermal conductivi-

ties. We can then use this effective thermal conductivity instead of the physical one to perform a purely thermal simulation while accounting for the convective influence. Although this produces local errors, the effects on the global solution should be negligible (Bejan, 1979, 2013; Manzano et al., 2016; Siavashi & Jamali, 2016; Börsing et al., 2017). This approach has three major advantages: First, we significantly reduce the compute time by transferring the hyperbolic PDE into an elliptic PDE. Second, we can use the certified RB method for all analyses since we no longer have a hyperbolic PDE. This should lead, to another significant reduction in compute time, as we demonstrated in this paper. Third, we can use the mismatch between simulation results, with the effective thermal conductivities, and the observation data to identify convection areas. This is of extreme relevance for regional hydrothermal investigations since more detailed physical modeling approaches can solely focus on this area.

Another source of uncertainty is related to the quality of the temperature measurements. Here, we focus on the principle applicability of the model calibration method and accept the data quality as given. Details related to the database for the observed temperatures and any permissions to use the latter need to be obtained from HLNUG.

5. Conclusion

We performed systematic geothermal model calibrations and sensitivity studies and showed, that only the model calibration in combination with the global sensitivity results in a both robust and reliable model calibration that can be used to identify model errors and possibly to compensate for these errors at a later stage.

We can not only identify the areas with unaccounted physical processes but can furthermore quantify their influence on the thermal conductivity. This is the reason why we are able to construct a conductive model that is able to compensate for the errors in the underlying physics, resulting in a model that can provide more reliable predictions, although not accounting for all relevant phys-

ical processes. The combination of a global sensitivity study and an automated model calibration is computationally prohibitive with state-of-the-art finite element simulations for high-resolution models, like basin-scale geothermal models as investigated here. Therefore, we use the RB method as a surrogate model, for the inverse processes. This reduces the compute time from 36 core-a to 10 core-min plus the initial cost of the generation of the surrogate model. However, the surrogate model can be re-used for other analyses.

Note that the calibration showed that for the upper two layers of the model we clearly see that the current model does not suffice. Furthermore, the RB method provides only error bounds for conductive geothermal models and not or convective models. Nonetheless, we demonstrated that the method is extremely promising to identify model discrepancy and to determine the dominant model parameters.

Acknowledgement

References

Agemar, T., Brunken, J., Jodocy, M., Schellschmidt, R., Schulz, R., & Stober, I. (2013). Untergrundtemperaturen in Baden-Württemberg. *Zeitschrift der Deutschen Gesellschaft für Geowissenschaften*, *164*, 49–62.

Agemar, T., Weber, J., & Schulz, R. (2014). Deep geothermal energy production in Germany. *Energies*, *7*, 4397–4416.

Baroni, G., & Tarantola, S. (2014). A General Probabilistic Framework for uncertainty and global sensitivity analysis of deterministic models: A hydrological case study. *Environmental Modelling & Software*, *51*, 26–34.

Barrault, M., Maday, Y., Nguyen, N. C., & Patera, A. T. (2004). An empirical interpolation method: application to efficient reduced-basis discretization of partial differential equations. *Comptes Rendus Mathematique*, *339*, 667–672.

Bauer, J. F., Meier, S., & Philipp, S. L. (2015). Architecture, fracture system, mechanical properties and permeability structure of a fault zone in Lower Triassic sandstone, Upper Rhine Graben. *Tectonophysics*, *647*, 132–145.

Bayer, U., Scheck, M., & Koehler, M. (1997). Modeling of the 3D thermal field in the northeast German basin. *Geologische Rundschau*, *86*, 241–251.

Bejan, A. (1979). A study of entropy generation in fundamental convective heat transfer. *Journal of Heat Transfer*, *101*, 718–725.

Bejan, A. (2013). *Convection heat transfer*. John wiley & sons.

Börsing, N., Wellmann, J. F., Niederau, J., & Regenauer-Lieb, K. (2017). Entropy production in a box: Analysis of instabilities in confined hydrothermal systems. *Water Resources Research*, *53*, 7716–7739.

Branch, M. A., Coleman, T. F., & Li, Y. (1999). A subspace, interior, and conjugate gradient method for large-scale bound-constrained minimization problems. *SIAM Journal on Scientific Computing*, *21*, 1–23.

Buchmann, T. J., & Connolly, P. T. (2007). Contemporary kinematics of the Upper Rhine Graben: a 3D finite element approach. *Global and Planetary Change*, *58*, 287–309.

Cacace, M., Blöcher, G., Watanabe, N., Moeck, I., Börsing, N., Scheck-Wenderoth, M., Kolditz, O., & Huenges, E. (2013). Modelling of fractured carbonate reservoirs: outline of a novel technique via a case study from the Molasse Basin, southern Bavaria, Germany. *Environmental earth sciences*, *70*, 3585–3602.

Campolongo, F., Cariboni, J., & Saltelli, A. (2007). An effective screening design for sensitivity analysis of large models. *Environmental modelling & software*, *22*, 1509–1518.

Cannavó, F. (2012). Sensitivity analysis for volcanic source modeling quality assessment and model selection. *Computers & geosciences*, *44*, 52–59.

Cloke, H., Pappenberger, F., & Renaud, J.-P. (2008). Multi-method global sensitivity analysis (MMGSA) for modelling floodplain hydrological processes. *Hydrological Processes: An International Journal*, *22*, 1660–1674.

Degen, D., Veroy, K., & Wellmann, F. (2020). Certified reduced basis method in geosciences. *Computational Geosciences*, *24*, 241–259.

Deutscher Wetterdienst (2020). Climate monitoring Germany. `https://www.dwd.de/EN/climate_environment/climatemonitoring/germany/germany_node.html`.

Fernández, M., Eguía, P., Granada, E., & Febrero, L. (2017). Sensitivity analysis of a vertical geothermal heat exchanger dynamic simulation: Calibration and error determination. *Geothermics*, *70*, 249–259.

Freymark, J., Bott, J., Cacace, M., Ziegler, M., & Scheck-Wenderoth, M. (2019). Influence of the Main Border Faults on the 3D Hydraulic Field of the Central Upper Rhine Graben. *Geofluids*, *2019*.

Freymark, J., Sippel, J., Scheck-Wenderoth, M., Bär, K., Stiller, M., Fritsche, J.-G., & Kracht, M. (2017). The deep thermal field of the Upper Rhine Graben. *Tectonophysics*, *694*, 114–129.

GeORG-Projektteam (2013). Geopotenziale des tieferen Untergrundes im Oberrheingraben. *Fachlich- Technischer Abschlussbericht des INTERREG- Projekts GeORG, Teil 1, LGRB-Informationen*, *28*, 1–104.

Geothermie, P. T. (2007). Nutzungen der geothermischen energie aus dem tiefen Untergrund (tiefe Geothermie)–arbeitshilfe für Geologische Dienste.

van Griensven, A. v., Meixner, T., Grunwald, S., Bishop, T., Diluzio, M., & Srinivasan, R. (2006). A global sensitivity analysis tool for the parameters of multi-variable catchment models. *Journal of hydrology*, *324*, 10–23.

Herman, J., & Usher, W. (2017). Salib: an open-source python library for sensitivity analysis. *J. Open Source Softw*, *2*, 97.

Hesthaven, J. S., Rozza, G., Stamm, B. et al. (2016). *Certified reduced basis methods for parametrized partial differential equations*. SpringerBriefs in Mathematics, Springer.

Houghton, J. T., Ding, Y., Griggs, D. J., Noguer, M., van der Linden, P. J., Dai, X., Maskell, K., & Johnson, C. (2001). *Climate change 2001: the scientific basis*. The Press Syndicate of the University of Cambridge.

Illies, J. (1972). The Rhine graben rift system-plate tectonics and transform faulting. *Geophysical surveys*, *1*, 27–60.

Jones, E., Oliphant, T., & Peterson, P. (2014). {SciPy}: Open source scientific tools for {Python}, .

Kolditz, O., & Clauser, C. (1998). Numerical simulation of flow and heat transfer in fractured crystalline rocks: application to the hot dry rock site in Rosemanowes (UK). *Geothermics*, *27*, 1–23.

Konrad, F., Savvatis, A., Wellmann, F., & Zosseder, K. (2019). Hydraulic behavior of fault zones in pump tests of geothermal wells: a parametric analysis using numerical simulations for the Upper Jurassic aquifer of the North Alpine Foreland Basin. *Geothermal Energy*, *7*, 1–28.

Lehmann, H., Wang, K., & Clauser, C. (1998). Parameter identification and uncertainty analysis for heat transfer at the KTB drill site using a 2-D inverse method. *Tectonophysics*, *291*, 179–194.

Manzano, G., Galve, F., Zambrini, R., & Parrondo, J. M. (2016). Entropy production and thermodynamic power of the squeezed thermal reservoir. *Physical Review E*, *93*, 052120.

Meixner, J., Schill, E., Grimmer, J. C., Gaucher, E., Kohl, T., & Klingler, P. (2016). Structural control of geothermal reservoirs in extensional tectonic

settings: an example from the Upper Rhine Graben. *Journal of Structural Geology*, *82*, 1–15.

Morris, M. D. (1991). Factorial sampling plans for preliminary computational experiments. *Technometrics*, *33*, 161–174.

Murphy, J. M., Sexton, D. M., Barnett, D. N., Jones, G. S., Webb, M. J., Collins, M., & Stainforth, D. A. (2004). Quantification of modelling uncertainties in a large ensemble of climate change simulations. *Nature*, *430*, 768–772.

Pauwels, H., Fouillac, C., & Fouillac, A.-M. (1993). Chemistry and isotopes of deep geothermal saline fluids in the Upper Rhine Graben: Origin of compounds and water-rock interactions. *Geochimica et Cosmochimica Acta*, *57*, 2737–2749.

Prud'homme, C., Rovas, D. V., Veroy, K., Machiels, L., Maday, Y., Patera, A. T., & Turinici, G. (2002). Reliable real-time solution of parametrized partial differential equations: Reduced-basis output bound methods. *Journal of Fluids Engineering*, *124*, 70–80.

Randolph, J. B., & Saar, M. O. (2011). Combining geothermal energy capture with geologic carbon dioxide sequestration. *Geophysical Research Letters*, *38*.

Ray, S., Mukherjee, J., & Mandal, S. (2015). Modelling nitrogen and carbon cycles in Hooghly estuary along with adjacent mangrove ecosystem. In *Developments in Environmental Modelling* (pp. 289–320). Elsevier volume 27.

Refsgaard, J. C., van der Sluijs, J. P., Højberg, A. L., & Vanrolleghem, P. A. (2007). Uncertainty in the environmental modelling process–a framework and guidance. *Environmental modelling & software*, *22*, 1543–1556.

Saltelli, A. (2002). Making best use of model evaluations to compute sensitivity indices. *Computer physics communications*, *145*, 280–297.

Saltelli, A., Annoni, P., Azzini, I., Campolongo, F., Ratto, M., & Tarantola, S. (2010). Variance based sensitivity analysis of model output. Design and

estimator for the total sensitivity index. *Computer Physics Communications*, *181*, 259–270.

Saltelli, A., Tarantola, S., Campolongo, F., & Ratto, M. (2004). Sensitivity analysis in practice: a guide to assessing scientific models. *Chichester, England*, .

Siavashi, M., & Jamali, M. (2016). Heat transfer and entropy generation analysis of turbulent flow of TiO2-water nanofluid inside annuli with different radius ratios using two-phase mixture model. *Applied Thermal Engineering*, *100*, 1149–1160.

Sobol, I. M. (2001). Global sensitivity indices for nonlinear mathematical models and their Monte Carlo estimates. *Mathematics and computers in simulation*, *55*, 271–280.

Song, X., Zhang, J., Zhan, C., Xuan, Y., Ye, M., & Xu, C. (2015). Global sensitivity analysis in hydrological modeling: Review of concepts, methods, theoretical framework, and applications. *Journal of hydrology*, *523*, 739–757.

Stober, I., & Bucher, K. (2015). Hydraulic and hydrochemical properties of deep sedimentary reservoirs of the Upper Rhine Graben, Europe. *Geofluids*, *15*, 464–482.

Tang, Y., Reed, P., Van Werkhoven, K., & Wagener, T. (2007). Advancing the identification and evaluation of distributed rainfall-runoff models using global sensitivity analysis. *Water Resources Research*, *43*.

Turcotte, D. L., & Schubert, G. (2002). *Geodynamics*. Cambridge university press.

Vidal, J., & Genter, A. (2018). Overview of naturally permeable fractured reservoirs in the central and southern Upper Rhine Graben: Insights from geothermal wells. *Geothermics*, *74*, 57–73.

Vidal, J., Genter, A., Schmittbuhl, J., Whitechurch, H., Baujard, C., & Damalais, E. (2015). Evolution of concepts for the geothermal projects in the Upper Rhine Graben. In *European Geothermal Workshop, Strasbourg, France*.

Vogt, C., Mottaghy, D., Wolf, A., Rath, V., Pechnig, R., & Clauser, C. (2010). Reducing temperature uncertainties by stochastic geothermal reservoir modelling. *Geophysical Journal International*, *181*, 321–333.

Wagner, R., & Clauser, C. (2005). Evaluating thermal response tests using parameter estimation for thermal conductivity and thermal capacity. *Journal of Geophysics and Engineering*, *2*, 349–356.

Wainwright, H. M., Finsterle, S., Jung, Y., Zhou, Q., & Birkholzer, J. T. (2014). Making sense of global sensitivity analyses. *Computers & Geosciences*, *65*, 84–94.

Wellmann, F., & Caumon, G. (2018). 3-D Structural geological models: Concepts, methods, and uncertainties. *Advances in Geophysics*, *59*, 1–121.

Zhan, C.-S., Song, X.-M., Xia, J., & Tong, C. (2013). An efficient integrated approach for global sensitivity analysis of hydrological model parameters. *Environmental Modelling & Software*, *41*, 39–52.